Unterschrift des Betreuers

TECHNISCHE
UNIVERSITÄT
WIEN

Diplomarbeit

EROSION OF TUNGSTEN-NITRIDE AND IRON-TUNGSTEN SURFACES UNDER DEUTERIUM ION IMPACT

Ausgeführt am Institut für
Angewandte Physik
der Technischen Universität Wien
Wiedner Hauptstraße 8-10 / 134
1040 Wien

unter der Anleitung von
Univ.Prof. Dr. **Friedrich AUMAYR**

und
Dipl.-Ing. **Bernhard Maximilian BERGER** BSc.

durch
Ing. **Reinhard STADLMAYR** BSc.
Scheugasse 1/13
1100 Wien

Wien, Februar 2016

(Reinhard Stadlmayr)

Kurzfassung

Kernfusion. Der heilige Gral der sauberen Energiegewinnung.
Viele physikalische und technische Probleme sind noch zu lösen, bevor ein Kernfusionskraftwerk gebaut werden kann. Einer der problematischsten Komponenten eines solchen Kraftwerks ist die Beschichtung der inneren Reaktorwand, welche in direkten Kontakt mit dem Fusionsplasma kommt. Die Suche nach Materialien, die den dort herschenden Bedingungen standhalten können, ist daher ein großes Forschungsgebiet.
Wolfram (W) ist ein vielversprechender Kandidat und wird bereits in vielen Forschungsreaktoren verwendet. Man hat bei diesen festgestellt, dass das Einbringen von Stickstoff (N) in das Fusionsplasma die thermische Belastung der Reaktorwand reduziert, insbesondere im Bereich des Divertors. N-Ionen Implantation führt aber zur Bildung von Wolfram-Nitride (WN) Schichten in der Reaktorwand, welche den Wandverschleiß verändern. Die Untersuchung der Zerstäubungsausbeuten von WN Schichten unter Deuterium (D) Ionen Bombardement ist daher von großem Interesse.
Weiters sollen für zukünftige Reaktoren sogenannte niedrig-aktivierbare Stähle (z.b. EUROFER) verwendet werden, welche neben Eisen (Fe) auch geringe Mengen an W enthalten (FeW). Unter Ionenbeschuss erfolgt präferentielles Sputtern, welches zu einer Anreicherung von W an der Oberfläche führt und dadurch den Materialverschleiß deutlich reduzieren könnte, welches wiederum die Lebensdauer der Reaktorwand deutlich erhöhen könnte.
Im Zuge dieser Arbeit wurden Messungen von Zerstäubungsausbeuten von W und WN Oberflächen, als auch von Fe und FeW Oberflächen, unter hohen D-Ionen Fluenzen ($\approx 10^{23}\,\mathrm{D/m^2}$), mithilfe einer hochempfindlichen Quartz-Kristall Mikrowaage, durchgeführt.
Eine bestehende ECR Ionenquelle erreicht nicht die notwendigen Ionenflüsse, um diese Hoch-Fluenz Messungen in akzeptabler Zeit durchzuführen, daher musste ein neues Setup entwickelt werden. Mit Hilfe der Verwendung eine Sputter-Gun konnte der Ionenfluss um ca. das 250 fache erhöht werden, wodurch nun Hoch-Fluenz Messungen möglich sind.
Die Messungen mit WN Oberflächen zeigen eine Abhängigkeit der Zerstäubungsausbeute von der aufgebrachten Fluenz. Ein anfangs erhöhte Zerstäubungsausbeute sinkt kontinuierlich, bis diese, bei höheren Fluenzen den gleichen Wert erreicht, wie jene von reinen W Oberflächen. Bei einer kinetischen Energie der D Ionen von $1000\,\mathrm{eV/D}$ wird dies nach einer Fluenz von $6\cdot 10^{22}\,\mathrm{D/m^2}$ erreicht und bei $500\,\mathrm{eV/D}$ ist die notwendige Fluenz mit $2\cdot 10^{22}\,\mathrm{D/m^2}$ deutlich geringer. Ein Vergleich dieser Messungen mit numerischen Simulationen durch SDTRIM.SP zeigen eine präferenzielle Abreicherung von N aus der Probe.
Die Zerstäubungsausbeute der FeW Oberflächen zeigen bei niedrigen Fluenzen den gleichen Wert als jene von reinem Fe, aber bei höheren Fluenzen ist ein deutliches Absinken zu sehen. Bei einer kinetischen Energie der D Ionen von $1000\,\mathrm{eV/D}$ ist nach einer Fluenz von $2\cdot 10^{23}\,\mathrm{D/m^2}$ eine nahezu konstante Zerstäubungsausbeute erkennbar. Bei $250\,\mathrm{eV/D}$ kann sogar nach einer Fluenz von $3.5\cdot 10^{23}\,\mathrm{D/m^2}$ noch ein Absinken der Zerstäubungsausbeute gemessen werden.

Abstract

Nuclear Fusion. The holy grail of clean energy production.

Still a lot of physical and technical issues need to be solved in order to use nuclear fusion as a future energy source. One of the most challenging parts is the coating of the reactor vessel, which faces the ultra hot plasma. The erosion of material compositions, used in nuclear fusion devices as a first boundary between the plasma and the reactor vessel, is therefore a topic of current research.

Current experimental nuclear fusion devices with a full tungsten divertor uses nitrogen seeding to reduce the power load on highly exposed surfaces, by enhanced radiative cooling. The formation of tungsten-nitride (WN) layers, caused by nitrogen (N) ion implantation and their erosion due to deuterium (D) and nitrogen (N) bombardment is therefore of particular interest.

For future fusion devices low activation steels (e.g. EUROFER) are considered for recessed areas. Preferential sputtering of tungsten-containing steels (FeW) could lead to a surface enrichment with tungsten (W), thereby reducing the erosion yield and increasing the lifetime of these components. A profound understanding of the interaction of D ions with WN and FeW surfaces is hence highly desirable.

In the course of this work W and WN surfaces, as well as Fe and FeW surfaces were bombarded with mono energetic D particles to measure sputter yields at high fluences ($\approx 10^{23}\,\mathrm{D/m^2}$), using a highly sensitive quartz crystal microbalance technique (QCM) under well defined laboratory conditions.

An existing ECR ion source was not able to provide sufficient high ion fluxes to do these measurements in an acceptable amount of time, so a new measurement setup needed to be developed. The use of a sputter gun as an ion source increases the ion flux by a factor of about 250, up to $2.7 \cdot 10^{18}\,\mathrm{D/m^2/s}$ and makes high fluence measurements feasible.

Measurements with WN surfaces show a strong dependence of the observed mass change rate on the bombarding D fluence. The mass loss is initially higher, compared to pure W surfaces, and drops with increasing fluence, reaching the same mass removal rate as for pure W. At a kinetic projectile energy of $1000\,\mathrm{eV/D}$ a fluence of about $6 \cdot 10^{22}\,\mathrm{D/m^2}$ is necessary, while at $500\,\mathrm{eV/D}$ the required fluence is with about $2 \cdot 10^{22}\,\mathrm{D/m^2}$ lower. Comparisons with dynamic sputtering calculations with SDTRIM.SP indicate a preferential removal of N and therefore a W enrichment of the surface.

The interaction of D projectiles with FeW surfaces, with $1.5\,\mathrm{at.}\ \%$ W, show at low fluences a mass removal rate close to the value of pure Fe. With increasing D fluence a reduction of the mass removal rate is observed. At a kinetic projectile energy of $1000\,\mathrm{eV/D}$ and after a bombarding fluence of $2 \cdot 10^{23}\,\mathrm{D/m^2}$ a nearly steady state mass removal rate can be seen. At $250\,\mathrm{eV/D}$ even after a fluence of about $3.5 \cdot 10^{23}\,\mathrm{D/m^2}$ no steady state conditions of the mass removal rate is found, a fact, which indicates a continuous surface enrichment of W.

Contents

1 Introduction **1**
- 1.1 Nuclear Fusion 1
- 1.2 Motivation and Outline 4
  - 1.2.1 Motivation for Investigation of WN Surfaces and development of a High Fluence Setup 4
  - 1.2.2 Motivation for Investigation of FeW Surfaces 5
- 1.3 List of Publications 6

2 Sputtering by Particle Bombardment **7**
- 2.1 General Physical Sputtering 7
- 2.2 Preferential Sputtering 9
- 2.3 The Quartz Crystal Microbalance Technique (QCM) 9
- 2.4 Numerical Simulations 11

3 Experimental Setup Development **13**
- 3.1 Experimental Setup with Wien Velocity Filter 13
  - 3.1.1 Mass Spectra Measurements 17
- 3.2 Experimental Setup without Wien Velocity Filter 20
  - 3.2.1 Mass Spectra Measurements 25
- 3.3 QCM Sample Holder 27
  - 3.3.1 Version 2011 27
  - 3.3.2 Version 2014, 2015 29
- 3.4 General Sputteryield Measuring Process 30
- 3.5 Error Estimation and Propagation 32
  - 3.5.1 Ion Current Density 32
  - 3.5.2 Resonance Frequency 34
  - 3.5.3 Sputter Yield Error 36
- 3.6 Sputtering of W by D Comparison Measurment 37
  - 3.6.1 Discussion 39

4 Transient Effects during Sputtering of WN by D **40**
- 4.1 Preparation of W an WN Samples 40
- 4.2 Sputtering of W by D 41
- 4.3 Sputtering of WN by D 43

5 Transient Effects during Sputtering of FeW by D **49**
5.1 Preparation of Fe and FeW Samples 49
5.2 Sputtering of Fe by D 49
5.2.1 Angle of Incidence Dependent Sputtering of Fe by D 51
5.3 Sputtering of FeW by D 53

6 Summary and Outlook **56**

Acronyms **i**

Bibliography **iii**

Danksagung **viii**

1 Introduction

The increasing energy demand of our modern world and the problem of global warming due to burning of fossil fuels require a rethinking of our energy production and consumption. Nuclear power is a possible solution, as it can deliver huge amounts of energy and is climate friendly, as no greenhouse gases are set free.

Nuclear energy can be gained either by fission of a very heavy nucleus, such as uranium-235, plutonium-239 or thorium-232, into two lighter nuclei or by fusion of two light nuclei, such as hydrogen-2 (deuterium) and hydrogen-3 (tritium), into a heavier one.

Fission power plants are working well, but the fission products are mostly highly radioactive and poisonous isotopes, like caesium-137, strontium-90, krypton-85, as well as long living radioactive isotopes like zirconium-93, caesium-135, palladium-107 and iodine-129. The storage of this fission waste is still an unsolved problem, because of the very high half-life of more than thousands of years of some of these isotopes. Accidents in the nuclear power plant in Chernobyl in 1986 and in Fukushima Daiichi in 2011 caused long term contamination of the surrounding area with these isotopes and therefore also a huge reduction of the public acceptance of fission power plants.

A nuclear fusion power station, in contrast, cannot produce any long living radioactive isotopes from fusion fuel, due to the underlying physical principle. Although materials used in the reactor chamber will be activated through neutron bombardment or by implantation of the fusion fuel tritium in the reactor wall, the radioactive waste will consist of rather short living isotopes only. Most of the activated material will be recyclable after a repository disposal of only a few decades [1].

Another advantage is, that fusion fuel is in principle in almost unlimited quantities accessible. The hydrogen isotope deuterium can be extracted out of water, while tritium can be gained by neutron bombardment of lithium, which is also commonly available.

These advantages would make a fusion power plant to an ideal source of energy. Nevertheless many technical and physical issues need to be solved in order to use nuclear fusion as a future energy source.

1.1 Nuclear Fusion

The binding energy per nucleon below masses of iron-56 is not saturated, according to the Bethe-Weizsäcker formula. Therefore the fusion of two very light nuclei into a heavier one is energetically favourable. To initialise nuclear fusion the two reactants need to reduce their distance to below $10^{-15}\,\mathrm{m}$. At this distance the strong interaction becomes effective and the two reactants fuse to a heavier nucleus. The total mass decreases in this reaction. This 'mass defect' is transformed into kinetic energy of the fusion products, according to $E = \Delta m \cdot c^2$. Bringing both reactants to this distances is challenging, because both nuclei are positively charged and therefore the repulsive force of the Coulomb interaction gets very strong at low distances. The fusing nuclei need a lot of kinetic energy to overcome this Coulomb barrier, or at least to tunnel through it. On Earth this is achieved by heating the fusion reactants to extremely high temperatures.

The most favourable fusion process, with highest reaction rate at lowest temperature, is the fusion of the hydrogen isotopes deuterium (D) and tritium (T):

$$^2_1D \;+\; ^3_1T \;\Rightarrow\; ^4_2He \;+\; ^1_0n \;+\; 17.6\,\mathrm{MeV}$$

This fusion process creates helium, a neutron and a net energy of $17.6\,\mathrm{MeV}$, spread as kinetic energy among both particles.

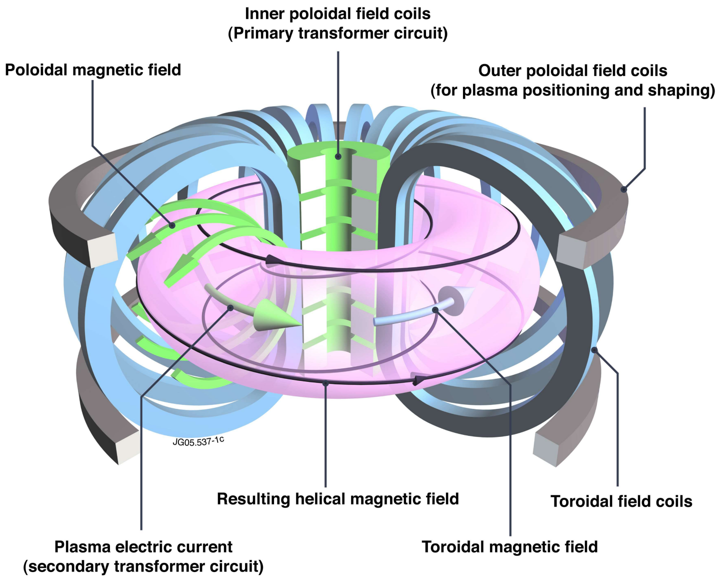

Figure 1.1 – TOKAMAK schematics, showing the magnetic field configuration and the confined plasma. Picture taken from [2].

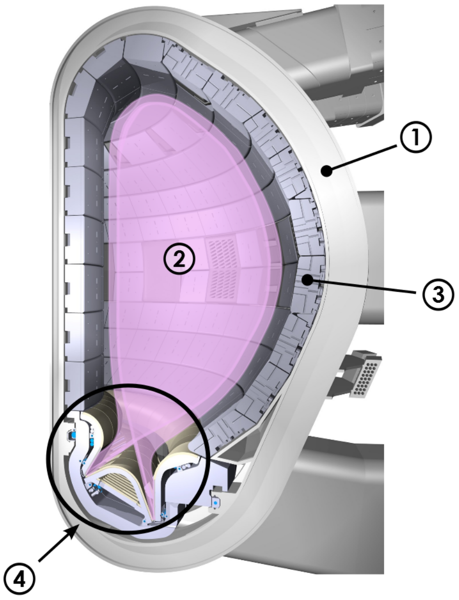

Figure 1.2 – Sectional drawing of ITER's TOKAMAK, showing a sketch of the plasma shape and the plasma facing components. Picture taken from [3].
① steel vacuum vessel
② deuterium tritium plasma
③ beryllium blankets
④ tungsten divertor

The most advanced concept for a nuclear fusion reactor is the TOKAMAK principle, which is based on the idea of magnetic confinement of the fusion fuel. A toroidal vacuum chamber is filled with the hydrogen isotope gas deuterium and tritium, to a density of $\approx 10^{20}\,\mathrm{particles/m^3}$ and heated up to $100-200$ million Kelvin, or $10-20\,\mathrm{keV}$ [3]. At these temperatures the gas fully ionises to a plasma and can be confined using strong magnetic fields. Figure 1.1 shows the magnetic field configuration in a TOKAMAK. A donut shaped reaction chamber is surrounded by toroidal field coils, generating a magnetic field inside the chamber. Additionally a solenoid in the center of the torus induces a toroidal plasma current. The resulting helical magnetic field constrains the ions to certain paths and confines the particles for a certain time. A self sustained fusion reaction can only occur, when the triple product of fuel density n_i, the energy confinement time τ_e and the plasma temperature T_i is high enough, according to the so called Lawson criterion [4].

For an extensive review of magnetically confined plasmas and the TOKAMAK principle see [2–6].

Still a lot of technical and physical issues need to be solved in order to use nuclear fusion as a future energy source. One of the most critically and technically challenging part of a fusion reactor is the coating of the vacuum chamber wall, which faces the ultra-hot plasma. Figure 1.2 shows a sectional drawing of the reactor chamber of the experimental nuclear fusion reactor ITER, which is currently under construction in france. An essential plasma facing component (PFC) in a fusion reactor is the so called divertor (figure 1.2,④). This device is located at the bottom of the torus, where the magnetic field lines touch the wall and allows shaping the plasma as well as separating the fusion ash helium from the fusion fuel. It is under continuous ion bombardment and therefore exhausted to highest heat load and erosion in the reactor [7, 8].

1.2 Motivation and Outline

A profound understanding of plasma-wall processes is crucial to use nuclear fusion as a future energy source. These interactions lead to sputtering of the reactor wall material, sputter redeposition, material mixing and also to chemical reactions with the wall material. These processes increase the erosion of the wall and limits the lifetime. Sputtering leads also to a contamination of the fuel-plasma with wall material, which can cause a cooling of the burning plasma and therefore to a disturbing of the fusion reaction [7, 9]. These effects must be minimized in a fusion power plant, to ensure stable long term energy production.

The interaction of the fusion fuel with the reactor wall can be approximated under laboratory conditions, by using a high flux ion source. Due to the fact that tritium is a radioactive material, investigations concentrate on deuterium.

This thesis is separated into three main parts. In the first part the development of a new experimental setup for high fluence measurements is described. The second and third part present sputter yield measurements of tungsten-nitride (WN) and iron-tungsten (FeW) surfaces by deuterium bombardment.

The motivation for each part is described in detail hereinafter.

1.2.1 Motivation for Investigation of WN Surfaces and development of a High Fluence Setup

Magnetic nuclear fusion experiments have shown, that impurity seeding into the plasma reduces high thermal stress load on the reactor wall due to radiative cooling and also increases the plasma performance [10, 11]. Current experimental nuclear fusion devices, like ASDEX Upgrade [10, 11], use a full tungsten (W) wall as a first physical boundary between the plasma and the reactor vessel. Other reactors, like JET [12, 13], and also future rectors, like ITER [14], will use W for the divertor and beryllium (Be) for the coating of the reactor vessel (figure 1.2). The use of nitrogen (N) as seeding gas reduces high local heat loads of the reactor wall and protects the divertor from thermal overload, but leads also to a N enrichment of the W wall (WN-layers) [10, 11].

The interacton of N ions with W and WN surfaces is well investigated and processes like sputtering of W and WN layers by N, N implantation and N retention are well studied [15–17]. On the other side only little is known about the interactions of deuterium (D) plasma with WN surfaces.

Numerical simulations with SDTRIM.SP have shown, that sputter yields of W and WN layers under D-ion bombardment reaches steady state conditions as soon as the bombarding fluence is high enough [18]. According to these simulations a D fluence of at least $10^{23}\,\mathrm{D/m^2}$ is necessary.

A D-ion source can be used to approximate the fusion fuel bombarding a sample-film of a possible reactor-wall material. The mass change of this material can then be measured,

using a highly sensitive quartz crystal microbalance technique, developed at the TU Wien (See chapter 2.3) [5, 19, 20].
The existing ECR-ion-source in the laboratory of the Institute of Applied Physics at the TU Wien, called SOPHIE [21], can deliver a D-ion flux of about $10^{16}\,\mathrm{D/m^2/s}$. To reach a fluence of $10^{23}\,\mathrm{D/m^2}$ would take approximately 2800 hours, or more than 100 days, which is not feasible [22]. Therefore a new measuring setup needed to be developed.
The idea was to use an existing sputter-gun (Type Perking Elmer PHI 04-261 2kV sputter ion gun) which can provide ion beam densities of up to $250\,\mu\mathrm{A/cm^2}$ at a gun-specimen distance of $2.5\,\mathrm{cm}$ [23]. Due to setup requirements this distance will be larger, but nevertheless this ion-source will significantly reduce the measuring time. Chapter 3 describes the development of this new measurement setup.
After that, this setup was used to study the interaction of mono-energetic D-ions with WN films of about $300\,\mathrm{nm}$. In chapter 4 the results of these measurements are presented and discussed.

1.2.2 Motivation for Investigation of FeW Surfaces

For a future fusion reactor, like DEMO, a stable and quiescent plasma has to be assumed. Hence the lifetime of the plasma facing components (PFC) will be limited by the plasma induced erosion, due to sputtering by ions and energetic neutrals. High-Z materials have considerable lower erosion rates than low-Z materials, especially at low ion energies impinging the PFCs. Some conceptual design studies for a future fusion power plant have proposed the use of tungsten containing steels for recessed areas of the PFCs [24, 25].
A presumed steady state operation of a future fusion power plant requires additionally excellent heat removal from the PFCs, to avoid thermal overload and therefore damage of the reactor wall. For this reason the bonding of the armor to the cooling components is essential, but also technologically challenging.
Tungsten containing steels, like EUROFER, could offer an alternative and are therefore of high interest for PFCs. Next to the base material iron (Fe) these steels contain some typical mid-Z elements, like chromium, vanadium and only a small amount of the high-Z element tungsten (W) [26, 27].
A main concern is the plasma induced erosion, which limits the lifetime of these plasma-facing steels and is therefore a topic of current research [27]. In recessed areas the erosion of the PFCs is mainly caused by ions and energetic neutrals with broad energy spectra, strongly peaking at low energies [27, 28]. Since the ion induced erosion rates of the high-Z element W is significantly lower compared to the mid-Z element Fe, the surface composition of these PFCs will change during ion bombardment. This causes surface enrichment of W due to preferential sputtering of Fe and reduces the total erosion rate [27]. Getting a better understanding of these surface enrichment processes of tungsten containing steels under D-ion bombardment is therefore highly desirable.
In this work the interaction of mono-energetic D ions with about $400\,\mathrm{nm}$ thick Fe and FeW

layers have been studied. As a model system for EUROFER steel, a FeW layer with $1.5\,\mathrm{at.\%}$ W has been chosen. In chapter 5 the results of these measurements are presented and discussed.

1.3 List of Publications

Parts of the results in this thesis have been presented as a poster and will be published in a scientific journal.

Publications in Scientific Journals:

- Berger B.M., Stadlmayr R., Meisl G., Cekada M., Eisenmenger-Sittner C., Schwarz-Selinger T., Aumayr F., "Transient effects during erosion of WN by deuterium ions studied with the quartz crystal microbalance technique", *Nuclear Instruments and Methods in Physics Research Section B* (2016)

Poster Presentations:

- Berger B.M., Stadlmayr R., Aumayr F., "Quantification of erosion rates of nitrogen saturated tungsten surfaces under deuterium ion impact", Sokendai Asian Winter School 2014, Toki/Japan

- Berger B.M., Stadlmayr R., Meisl G., Cekada M., Sugiyama K., Oberkofler M., Schwarz-Selinger T., Aumayr F., "Transient effects during erosion of WN and FeW films by deuterium ions studied with the quartz crystal microbalance technique", 15th International Conference on Plasma-Facing Materials and Components for Fusion Applications (PFMC-15), Aix-en-Provence/France

- Stadlmayr R., Berger B.M., Blöch D., Kaser S., Bergen L., Aumayr F., "Erosion of iron and iron-tungsten films under deuterium ion impact", Symposium on Surface Science 2016, St. Christoph am Arlberg/Austria

2 Sputtering by Particle Bombardment

Energetic ions or neutral particles hitting a solid or liquid surface transfer energy to the target via single or multiple elastic collisions with the target atoms. These collision cascades spread the kinetic energy of the projectiles in the target, which can lead to sputtering as soon as the recoil cascades reach the target surface. If an atom at the surface gains enough kinetic energy and linear momentum perpendicular to the surface, to overcome the surface binding energy E_{SB}, it can be ejected and is sputtered [5, 29, 30].
Next to this physical sputtering processes chemical sputtering can occur. Chemical reactions between the projectile and target element can strongly influence the sputtering behaviour of the target [5, 31].
Potential sputtering is another process leading to target mass changes, where the potential energy of an ion in the form of high ionisation states are used. The neutralisation of these ions can lead to sputtering too [5, 30, 32].

2.1 General Physical Sputtering

The sputter yield Y is defined as sputtered target atoms per incident projectile particle:

$$\mathrm{Y} = \frac{\text{sputtered atoms}}{\text{projectile particle}} \tag{2.1.1}$$

Y is dependent on the kinetic energy of the projectile, the mass ration of projectile and target elements, the angel of incidence of the projectiles, the surface binding energy and the target composition [29, 30].
The maximum amount of linear momentum and therefore kinetic energy can be transfered between two impact partners, if their mass ratio is 1 and gets less efficient with increasing mass difference, as can be seen in equation 2.1.2.

$$\frac{\Delta E}{E_1} = \frac{4m_1m_2}{(m_1+m_2)^2} \tag{2.1.2}$$

ΔE is the transfered energy from particle 1 to 2, E_1 the kinetic energy of particle 1 before the collision and $m_{1,2}$ the masses of the impact partners [30].
The kinetic energy of the projectile needs to be higher than a threshold energy E_{th} to initialize

sputtering. This energy depends on the mass difference between projectile and target, as well as the surface binding energy of the target. Figure 2.1 shows a typical energy dependence of the sputter yield of Fe and W by D. For sputtering Fe by D, the threshold energy is $\approx 41\,\mathrm{eV}$ and for sputtering W by D $\approx 229\,\mathrm{eV}$ [30]. Increasing the projectiles kinetic energy leads also to an increase of the sputter yield, until a certain maximum is reached. Further increase reduces the sputter yield again, because the collision cascades spread very deep into the target and hardly return back to the target surface [29, 30].

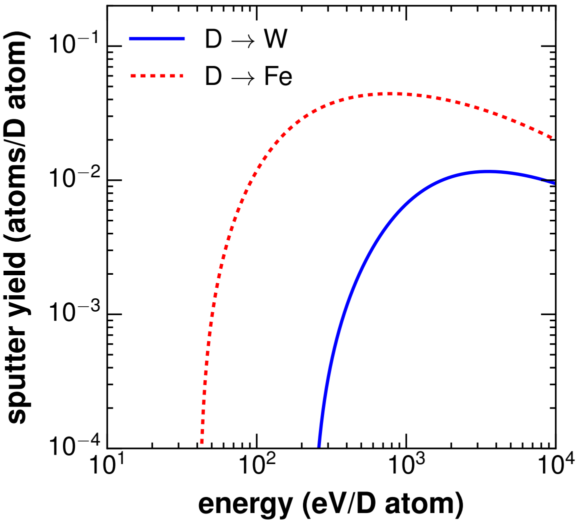

Figure 2.1 – D → W and D → Fe sputter yield as a function of the ion energy, calculated with SDTRIM.SP.

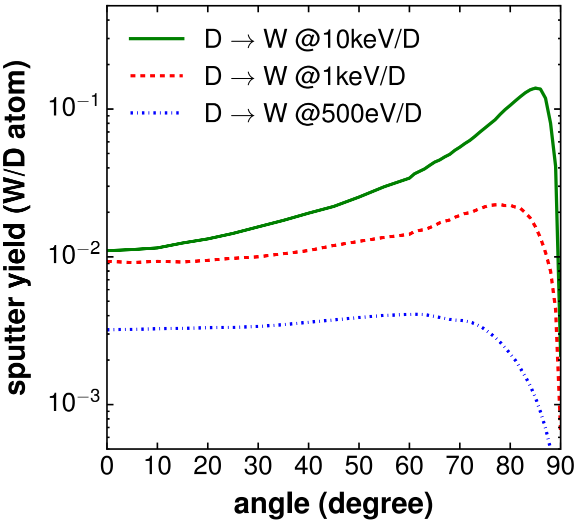

Figure 2.2 – D → W sputter yield as a function of the ion impact angle (with respect to the surface normal), calculated with SDTRIM.SP at different projectile energies.

Increasing the impact angle (with respect to the surface normal) usually increases the sputter yield (figure 2.3). The collision cascades stay more closer to the surface, which increases the probability, that surface atoms gain enough energy from these collision cascades to be sputtered. This effect is weak at low projectile energies and gets stronger with increasing kinetic energy of the projectile, as can be seen in figure 2.2. Getting closer to gracing incidence impact angles reduces the sputter yield again, because the projectiles are more and more reflected from the topmost surface layer and do not penetrate into the target [30] any more. The sputtering behaviour is, however, strongly affected by surface roughness, which is topic of current research.

For an extensive review of sputtering theory, see [5, 29–31].

2.2 Preferential Sputtering

Sputtering of multicomponent targets can show a more complex behaviour and is usually dependent on the bombarding fluence. Elemental depth distributions can change by particle bombardment and also the total sputter yield Y_{total}.
Y_{total} in an n-component target is defined as the sum over all partial sputter yields Y_i:

$$Y_{total} = \sum_{i=1}^{n} Y_i \tag{2.2.1}$$

A partial sputter yield Y_i is defined as sputtered atoms of component i per incident particle, equivalent to equation 2.1.1 and is not necessarily equivalent to the sputter yield of a pure target of component i [30].
In a multicomponent target the energy transfer between the projectile and the different target atoms, as well as between the target atoms themselves is less efficient with high mass differences, as can be seen in equation 2.1.2. Therefore the energy transfer is here more complex and the partial sputter yields are also dependent on the material concentration of the target [29, 30].
Bombarding a multicomponent target of materials with strongly different partial sputter yields can lead to effects, like preferential sputtering. Here the target components with higher sputter yield are preferably sputtered. This can lead to a surface enrichment of the target components with a lower sputter yield and cause a fluence dependent reduction of the total sputter yield. As soon as the partial sputter yields are equal, equilibrium is reached and the surface enrichment stops. Competing processes, like diffusion of material from deeper regions to the surface can counteract this enrichment effect [29, 30].
If the projectile energy is below the threshold energy for sputtering of one of the target materials, the effect of preferential sputtering can be very strong. For example a low amount of the high Z material W in Fe can strongly reduce the sputter erosion under low energy D bombardment. Under particle bombardment a layer of nearly pure W will develop at the target surface and reduce the total sputter yield, which is highly desired in fusion science and therefore topic of current research [27, 30].

2.3 The Quartz Crystal Microbalance Technique (QCM)

For investigating these sputtering effects a quartz crystal microbalance (QCM) can be used, which is an ideal tool to measure small mass changes.
The principle is based on the fact, that the thickness of a quartz crystal defines its resonance frequency. The thickness of the crystal is direct proportional to its mass. A change of this thickness is equal to a mass change and causes a change of the resonance frequency, which holds true for a thin film of a sample material deposited onto the quartz crystal [19, 20]. The so called Sauerbrey equation 2.3.1 is a good approximation for this effect [20]. It describes

the relation between the relative mass change and the relative change of the resonance frequency:

$$\frac{\Delta m}{m} = -\frac{\Delta f}{f} \tag{2.3.1}$$

The used technique was developed at the TU Wien and is especially designed for high sensitive sputteryield measurements under UHV conditions. It uses a stress compensated (SC-cut) quartz crystal disk (Type KVG Quartz Crystal Technology model XA3641), coated with a $140\,\mathrm{nm}$ gold electrode on each side. On one of these electrodes a thin film of some $100\,\mathrm{nm}$ of the sample material is deposited (compare with figure 2.3) [5, 19].
The highly sensitive driving electronics lead the quartz to oscillate in a thickness shear mode at its resonance frequency of about $6\,\mathrm{MHz}$, with a precision in the rage of mHz. This resonance frequency can be measured with a highly accurate frequency counter [5, 19, 20]. Ion bombardment of the target material lead to a mass change, which can then be measured as a change in the resonance frequency of the quartz.
This QCM technique allows in situ mass change measurements and can reach a sensitivity of $\frac{\Delta f}{f} \approx 10^{-9}$, which is equivalent to a mass change of $\approx 10^{-4}$ tungsten monolayers per second.

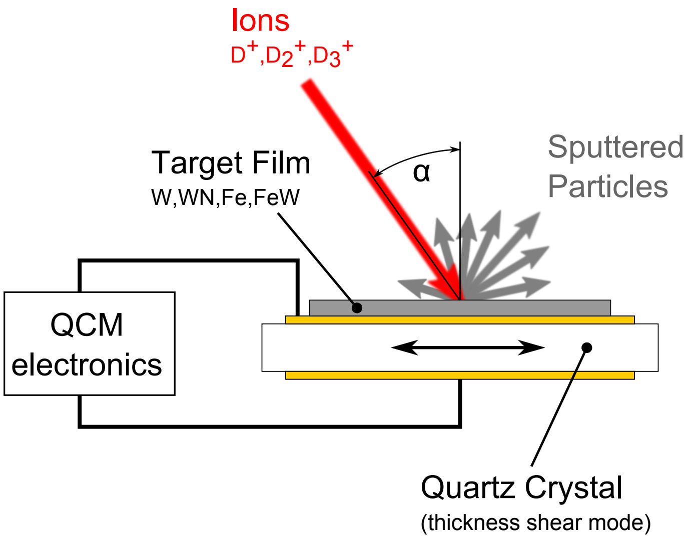

Figure 2.3 – QCM technique schematics:
Ions hit the surface of a coated quartz crystal under a certain angle of incidence α and with specific kinetic energy. The ion surface interaction lead to sputtering of the target film. The mass change can be measured as a change in the resonance frequency of the quartz crystal, which is used for sputter yield calculations.

Using the Sauerbrey equation 2.3.1, including the incident ion current and the time derivative of the frequency $\Delta f/\Delta t$, the mass removal rate y can be calculated:

$$y[\mathrm{amu/ion}] = C \cdot \frac{1}{j_{FC}} \cdot \frac{\Delta f}{\Delta t} \qquad \text{with} \quad C = \frac{\rho_Q \cdot l_Q \cdot q \cdot e}{f \cdot m_n} \tag{2.3.2}$$

Essential parameters are the frequency change over time $\Delta f / \Delta t$ and the ion current density j_{FC}, which need to be measured with high precision. C is a constant including the quartz crystal parameters, which can be found in table 2.1. The total sputter yield follows from $Y = y/m_i$, where m_i is the target particle mass [19].

Table 2.1 – QCM parameters from equation 2.3.2

ρ_Q	density of the quartz crystal
l_Q	thickness of the crystal
q	charge state of the working gas
e	elementary charge
m_n	atomic mass unit
f	resonance frequency of the crystal

In order to perform high precision sputter yield measurements, some other quartz crystal properties need to be taken into account:

The sensitivity of the quartz crystal is position dependent. The highest sensitivity is in the center of the crystal, where the oscillating amplitude has its maximum, and drops radially outwards [33]. Significant deviations from equation 2.3.1 can occur due to nonuniform mass remvoal, caused by an inhomogeneous ion beam. To avoid this, the ion beam need to be scanned over the entire area of the quartz crystal, to achieve a homogeneous areal mass change of the sample [19].

Besides this, the quartz crystals resonance frequency is sensitive to changes of the operating temperature. To minimize this effects, the quartz crystal need to be operated at the minimum of its frequency over temperature curve, which corresponds to a polynomial of cubic degree [5, 34]. This minimum need to be found for every sample by a careful temperature scan and is usually in the range of $430\,\mathrm{K} - 470\,\mathrm{K}$.

A stable and homogeneous ion beam as well as optimal operating conditions of the quartz crystal are therefore very important for QCM measurements.

For an extensive review of the QCM technique, see [5, 19, 20].

2.4 Numerical Simulations

Next to the experimental measurements, computer simulations are of great importance to get a better understanding of ion surface interactions. Ions hitting a target surface initialize collision cascades, which can cause sputtering. With a certain accuracy these effects can be simulated in software.

In this work the software SDTRIM.SP, version 5.07 is used. This program allows calculations of sputtering yields, reflection coefficients of static as well as dynamically changing targets. Dynamic targets are divided into finite layers and allow for thickness as well as composition changes, which can be calculated in dependence of the projectile particle fluence [35]. This allows simulations of effects, like preferential sputtering.

This software combines TRIM and TRIDYN, which are basic codes for simulating transport of ions in matter. They base on Monte Carlo simulations, assuming an amorphous target and use binary collision approximation (BCA) for the atomic collisions [36–38]. Here the particles are approximated to travel trough matter by experiencing a sequence of independent binary elastic collisions with the target atoms. Between the collision the particles travel in straight lines.

Sputtering of a surface atom occurs, as soon as its kinetic energy from the linear momentum perpendicular to the target surface $p_\perp$ is greater than its surface binding energy E_{SB}:

$$\frac{p_\perp^2}{2m} > E_{SB} \tag{2.4.1}$$

A crucial parameter in these simulations is the surface binding energy E_{SB}. For pure element this energy is known from sublimation energy measurements. For mixed materials, in contrast, the surface binding energy is more complicated, because it is dependent on the surface concentration of each material and therefore hard to measure. Usually models are needed here to calculate feasible surface binding energies [29, 30].

SDTRIM.SP may also include diffusion of materials, nevertheless effects like irradiation induced diffusion, chemical sputtering and changes in the surface topologies cannot be simulated jet.

For an extensive review of these numerical simulation techniques, see [35–40].

3 Experimental Setup Development

This chapter describes the development of a new measurement setup for high fluence sputtering measurements. Section 3.1 and 3.2 describes two setup configurations, with and without the use of a Wien velocity filter. In section 3.3 the different sample holder are presented, showing advantages and disadvantages of them. In section 3.4 the sputter yield measurement process is described and section 3.5 presents a rigorous error estimation. Section 3.6 presents test measurements and comparisons to literature data.

3.1 Experimental Setup with Wien Velocity Filter

The whole setup can be divided into three main sections: first the vacuum chamber including all devices to create and check the required vacuum environment, secondly the ion source including the ion beam preparation and thirdly the QCM sample holder with the measuring instruments. Figure 3.1 shows the schematics of this setup and figure 3.2 a 3D CAD drawing of it.

Vacuum Chamber: The measurements require ultra high vacuum (UHV) conditions. A base pressure of about $10^{-9}\,\mathrm{mbar}$ needs to be achieved in order to perform accurate measurements. The vacuum vessel itself is made of stainless steel components and uses Conflat flanges (CF) with copper gaskets. The pump setup consists of one rotary-vane pre-vacuum pump (Type Pfeiffer DUO 10M) and up to two turbo molecular high vacuum pumps (Type Pfeiffer TPU 240 with Pfeiffer TCP 121 power supply). The pre-vacuum pressure is measured with a Pirani gauge head (Type Pfeiffer TPR 010) and the base pressure in the chamber with two Penning gauge heads (Type Pfeiffer IKR 050). One is located close to the ion source, to measure the working gas pressure, and the second one nearby the QCM. All pressure gauges are controlled by a Pfeiffer Balzers TPG 300 vacuum gauge controller. To analyse the residual gas a quadrupole mass analyser (Type Pfeiffer QME 220) is used. As working gas source Linde HiQ®Minican gas bottles are used, in combination with a gas dosing control valve (Type Pfeiffer UDV 135 thermovalve with Pfeiffer RVG-050-B control).

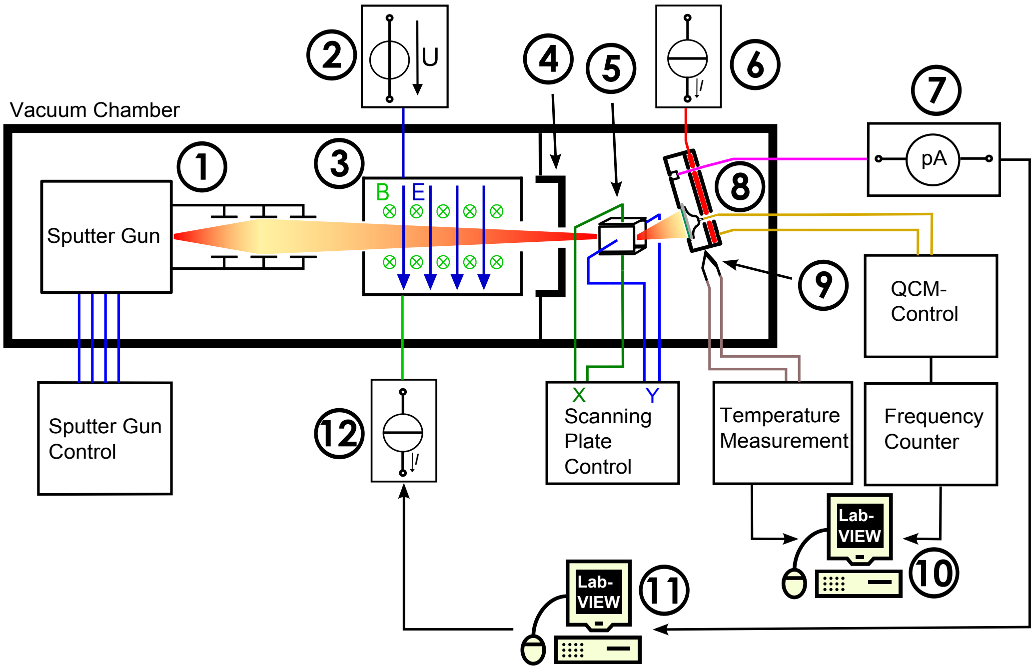

Figure 3.1 – experimental setup schematic with Wien velocity filter:
① ion source with einzel lens
② voltage supply for the deflection plates of the Wien velocity filter
③ Wien velocity filter
④ Ø $5\,\mathrm{mm}$ aperture
⑤ scanning and deflection plate pairs
⑥ constant current supply for the QCM temperature control
⑦ picoampere meter to measure the ion current through the FC
⑧ QCM holder with the quartz crystal sample and the FC
⑨ thermocouple for QCM temperature measurements
⑩ PC with LabVIEW to log the QCM frequency and the temperature
⑪ PC with LabVIEW to control the current supply to the Wien filter coils and to do automated mass spectra measurements
⑫ current supply for the Wien velocity filter magnet coils

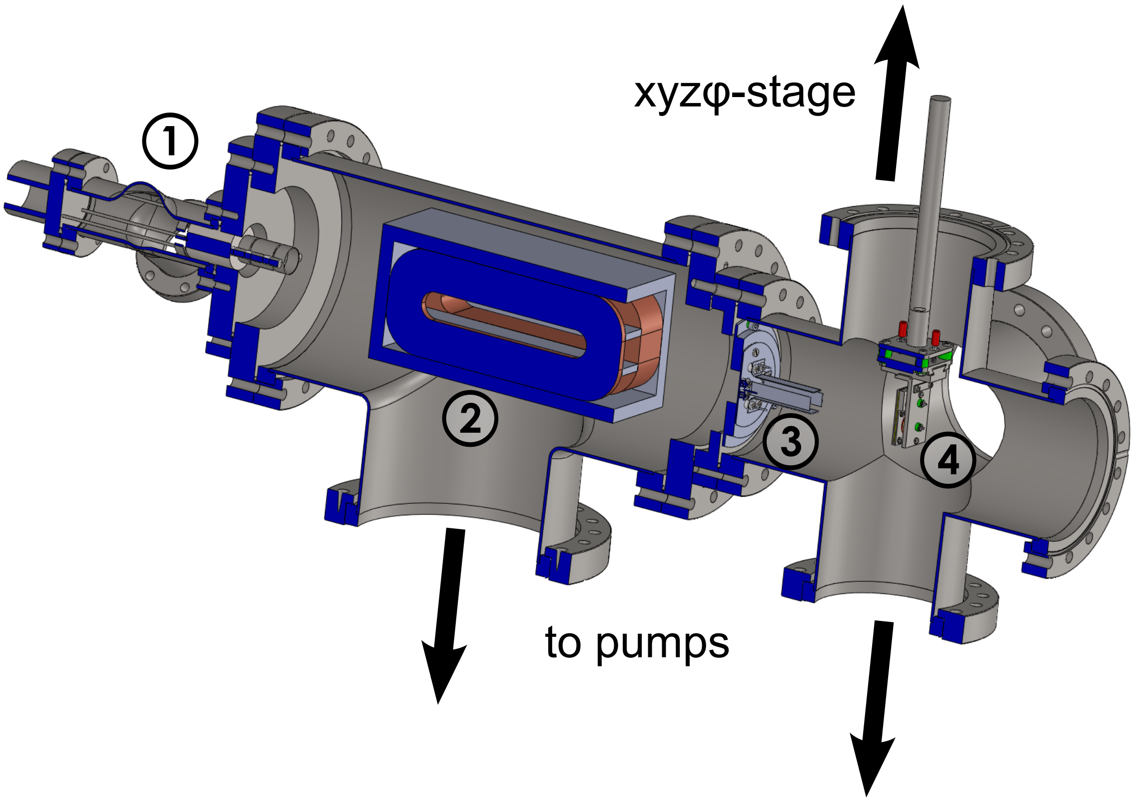

Figure 3.2 – sectional drawing of the measurement setup with Wien velocity filter:
① ion source with einzel lens
② Wien velocity filter
③ Ø $5\,\mathrm{mm}$ aperture with deflection plates
④ QCM holder with FC. The position can be adjusted with a xyzφ-stage.

Ion Source: The ion source (Type Perking Elmer PHI 04-261 2kV sputter ion gun) can generate a continuous ion beam with specific kinetic energy, according to the offered acceleration voltages of $0.5\,\mathrm{kV}$,$1\,\mathrm{kV}$,$1.5\,\mathrm{kV}$ or $2\,\mathrm{kV}$. An einzel lens on the front end of the ion source allows focusing the beam [23].

A Wien velocity filter (Type Colutron Velocity Filter, Model 600), equipped with a voltage supply for internal deflection plates ($\vec{E}$-field) and a current supply for internal deflection coils ($\vec{B}$-field), allows selecting the ions according to their speed of $v = |\vec{E}|/|\vec{B}|$ and therefore to their mass over charge ratio m/q [41].

Two pairs of deflection plates, arranged behind the velocity filter on top of a Ø $5\,\mathrm{mm}$ aperture, allow exact positioning of the ion beam onto the QCM sample holder. Additionally applied zigzag voltages are used to scan the ion beam over the whole active area of the QCM.

QCM Sample Holder and Measuring Instruments: A built in Faraday Cup (FC) in the QCM holder allows to measure the ion current with a picoampere meter (Type Keithley 6485 Picoamperemeter).

Ion source, velocity filter and the aperture with the deflection plate pairs are aligned perfectly. A fraction of the ion beam neutralizes, because of electron capture and is not longer effected by the Lorentz force. The ion beam as well as the neutral particle beam cause mass loss of the QCM, but the neutrals cannot be measured with the FC and would therefore falsify sputter yield measurements. This problem is solved by repositioning the QCM holder $9\,\mathrm{mm}$ away from the neutral ion beam axis (See figure 3.3) and by applying additional voltage to the deflection plates. Therefore only charged particles are deflected to the active area of the quartz crystal.

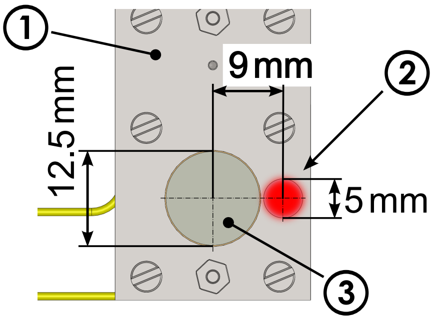

Figure 3.3 – Minimum distance to avoid neutral particles hitting the quartz sample.
① QCM holder, ② possible neutral particle beam, ③ quartz crystal sample

The QCM holder contains also a ohmic heater, which allows to operate the quartz crystal at different temperatures and is adjusted, using a constant current power supply. The temperature is measured using a K-type thermocouple and logged, using a PC with LabVIEW.

The QCM control drives and keeps the quartz crystal at its resonance frequency. This

frequency is measured with a frequency counter (Type Tektronix FCA3000 with TCXO reference frequency) and also logged, using a PC with LabVIEW.
For sputter yield measurements the ion current values are recorded manually, but for mass spectra measurements the picoampere meter current measurements were recorded by another PC with LabVIEW. This PC is able to control the current supply for the Wien velocity filter coils and allows fully automated mass spectra measurements.

3.1.1 Mass Spectra Measurements

Analysing the ion beam is crucial for accurate sputter yield measurements. Working gas impurities can falsify measurements, therefore the Wien velocity filter is used to perform mass spectra analysis of the ion beam. Additionally the possibility of a measurement setup without using a velocity filter at all is checked.

3.1.1.1 Mass Calculation:

Automated Wien velocity filter mass spectra measurements are performed by setting a constant $\vec{E}$ field and varying the $\vec{B}$ field or vice versa. Here the $\vec{E}$ Field was set constant, while the $\vec{B}$ field was varied, by increasing the current through the deflection coils according a programmed ramp. Continuous measurement of the ion current with a FC allows logging a ion current - Wien filter coil current dependence. A simple method to convert this data to a mass spectra is described hereinafter.

An ion with a kinetic energy of $E_{kin} = q \cdot V_{ACC}$ (q = charge state, V_{ACC} = acceleration voltage) passes the Wien velocity filter, if the Lorentz force compensates:

$$\vec{0} = \vec{F_L} = q(\vec{E} + \vec{v} \times \vec{B}) \quad \text{with} \quad \vec{E} \perp \vec{B} \perp \vec{v} \quad \text{and} \quad |\vec{E}| = E \quad |\vec{B}| = B \quad |\vec{v}| = v$$

The mass m follows from:

$$\Rightarrow \quad qE = qBv = qB\sqrt{\frac{2qV_{ACC}}{m}} \qquad \Rightarrow \qquad m = 2qV_{ACC}\frac{B^2}{E^2} \tag{3.1.1}$$

The magnetic field B is direct proportional to the current through the magnetic coils I. Including an offset current I_{offset}, to correct the zero position of the mass spectra and a constant factor C, the mass can be calculated as follows:

$$m = C \cdot (I - I_{offset})^2 \tag{3.1.2}$$

These parameters can be evaluated if two peaks from the ion current measurement can be identified immediately out of the measured spectra:

$$C = \frac{m_1}{(I_1 - I_{offset})^2} = \frac{m_2}{(I_2 - I_{offset})^2} \qquad \Rightarrow \qquad I_{offset} = \frac{I_1\sqrt{m_2} - I_2\sqrt{m_1}}{\sqrt{m_2} - \sqrt{m_1}} \tag{3.1.3}$$

Due to the fact that deuterium is used as working gas, the highest peak in the measurement is the D_2^+ ion with $m = 4\,\mathrm{amu}$ and can be used as first calibration point. The small amount of atomic D^+ ions with $m = 2\,\mathrm{amu}$ can be used as second calculation point, because it is the first significant ion current peak at the lower end of the Wien velocity filter coil current values.

3.1.1.2 Results:

In table 3.1 the setup configuration for the Wien filter mass spectra measurements is listed.

Table 3.1 – mass spectra measurement parameters

gas type	deuterium of 99.5% purity
ion source working gas pressure	$6 \cdot 10^{-5}\,\mathrm{mBar}$
ion source acceleration voltage	$+1000\,\mathrm{V}$
QCM holder version	2011
Wien velocity filter voltage	$+100\,\mathrm{V}$
Wien velocity filter current	$0\,\mathrm{A}$ to $3\,\mathrm{A}$

The ion current was measured with the FC in the QCM holder. The whole FC was kept on a $+50\,\mathrm{V}$ potential to avoid loosing electrons through secondary emission.

The current itself was measured with a picoampere meter and forwarded to a control PC with a LabVIEW program, which records the data and also controls the current supply of the Wien velocity filter coils. The current through the coils was increased form $0\,\mathrm{A}$ to $3\,\mathrm{A}$, in steps of $2\,\mathrm{mA}$.

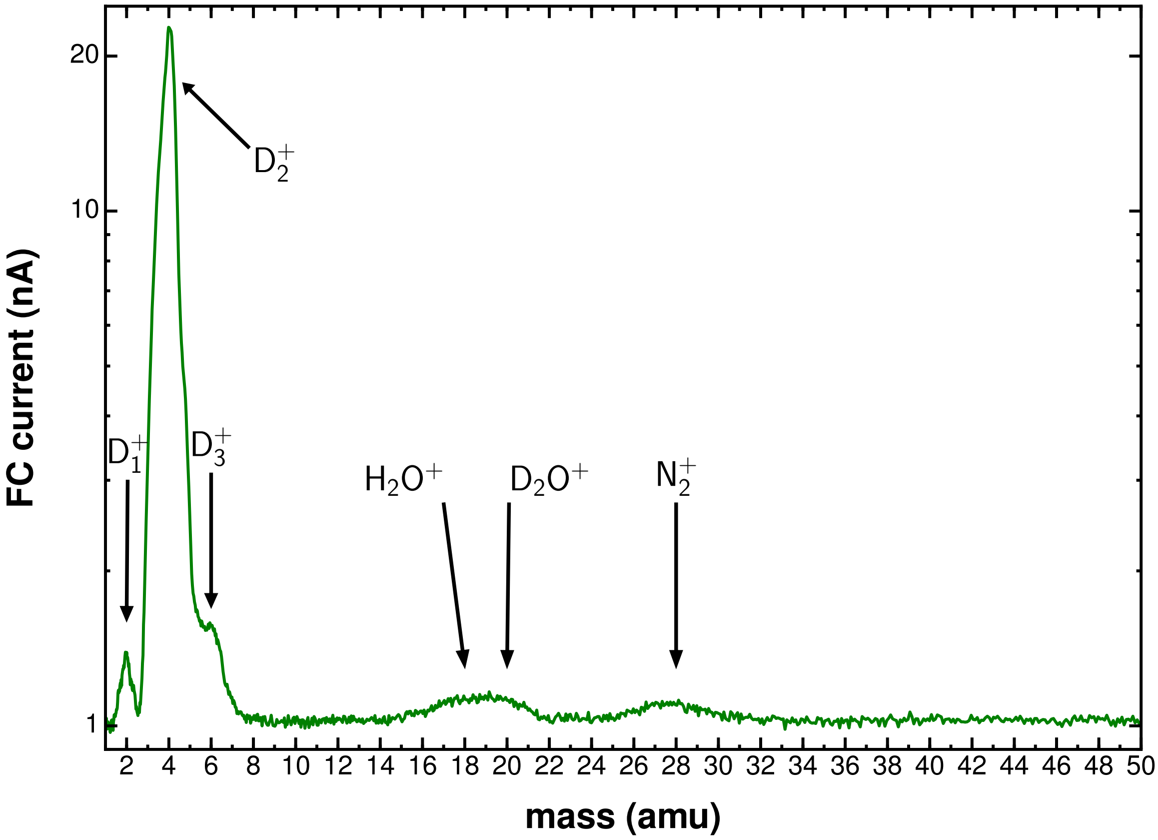

Figure 3.4 – Wien filter mass spectra, using a deuterium gas source of $99.5\,\%$ purity. The main peaks are caused by Deuterium, but also some higher mass ions, like water, heavy water and nitrogen can be seen. To improve the readability of this logarithmic graph, a constant ion current of $1\,\mathrm{nA}$ was added to the results.

Table 3.2 – Measured ion currents from figure 3.4.

mass [amu]	ion	FC current [nA]	in [%]
2	D^+	0.39	1.7
4	D_2^+	21.75	93.5
6	D_3^+	0.59	2.6
18	H_2O^+	0.13	0.5
19	HDO^+	0.16	0.7
20	D_2O^+	0.13	0.5
28	N_2^+	0.12	0.5

Figure 3.4 shows a mass spectrum and table 3.2 lists the ion current values from this mass spectrum. The measurement shows a low occurrence of heavy ions. Some minor peaks of

nitrogen and water ions, with a percentage of 2.3 could be detected, however the influence of these ions to the sputter yield measurements could be too high.
A short estimation: the sputter yield of deuterium ions bombarding a pure tungsten target at an energy of $1000\,\mathrm{eV/D}$ is $Y_{DW} = 6 \cdot 10^{-3}\,\mathrm{W/D}$ [30]. The sputter yield of nitrogen ions bombarding a pure tungsten target at the same energy is $Y_{NW} = 1.5 \cdot 10^{-1}\,\mathrm{W/ion}$ [15]. According to table 3.2 the amount of D_2 is $93.5\,\%$ and the amount of nitrogen $0.5\,\%$. Assuming an ion beam with these two components, the combined sputter yield Y_{DNW} can be estimated as the weighted average of both single ion sputter yields.

$$\frac{Y_{DNW}}{Y_{DW}} = \frac{Y_{DW} \cdot 0.935 + Y_{NW} \cdot 0.005}{(0.935 + 0.005) \cdot Y_{DW}} = 113\,\% \tag{3.1.4}$$

The resulting relative sputter yield is about $13\,\%$ higher than of a pure deuterium ion beam. For that reason the amount of heavy ions need to be lowered to make accurate sputter yield measurements if no velocity filter is used.
Baking the whole setup at higher temperatures would reduce the amount of these ions, but it is limited to $100\,^{\circ}\mathrm{C}$ to avoid damages on the Wien velocity filter. Therefore a setup without ion separation using a velocity filter should be possible, as long as the purity of the gas source is high enough.
Table 3.2 shows also, that the measured deuterium ion current is about $22\,\mathrm{nA}$. Activating the ion beam scanning, which is necessary to cover the whole sample area with a homogeneous ion current, reduces the ion current to $6.5\,\mathrm{nA}$. Considering the aperture size of the FC of $1.103\,\mathrm{mm}^2$, this current is equal to a flux of $7 \cdot 10^{16}\,\mathrm{D/m^2/s}$. To reach a fluence of $10^{23}\,\mathrm{D/m^2}$ would take about 17 days, which is already seven times better compared to SOPHIE, but is still too much. The ion beam divergence of the used ion sputter gun is quite high and due to the big distance between the ion source and the target, the ion current is relatively low.
Consequentially a setup without the Wien velocity filter would have the following advantages:

- Higher baking temperatures will decrease the amount of impurities, like water and nitrogen, which lead to a purer mass spectrum and therefore minimises sputter yield measurements errors.

- The reduced distance between the ion source and the target will decrease the effect of beam divergence and therefore increase the ion flux at the target, which will reduce the measuring time.

3.2 Experimental Setup without Wien Velocity Filter

A setup without the Wien velocity filter allows a significant reduction of the distance between the ion source and the QCM sample holder. The effect of the beam divergence is therefore less severe, which leads to an increase of the ion flux.

This setup largely corresponds with the experimental setup, described in chapter 3.1, but some extra modifications were necessary. Figure 3.5 shows the schematics of this measurement setup.

As can be seen in the CAD sectional drawing of the measurement setup (figure 3.6) the front end of the sputter gun extends into the CF100 6 way cross. Therefore the aperture from the previous experimental setup could not be reused and needed to be redesigned. The hat-like shape of this new aperture causes a reduction of the distance between the deflection plates and the QCM holder. Therefore a stronger $\vec{E}$-field between the deflection plates is necessary to deflect the ion beam, according to figure 3.3. The scanning plate control is not able to deliver a voltage high enough to generate a sufficient $\vec{E}$-field, so two additional voltage supplies were added to the horizontal pair of the plates.

Figure 3.7 shows a photograph of the whole measurement setup.

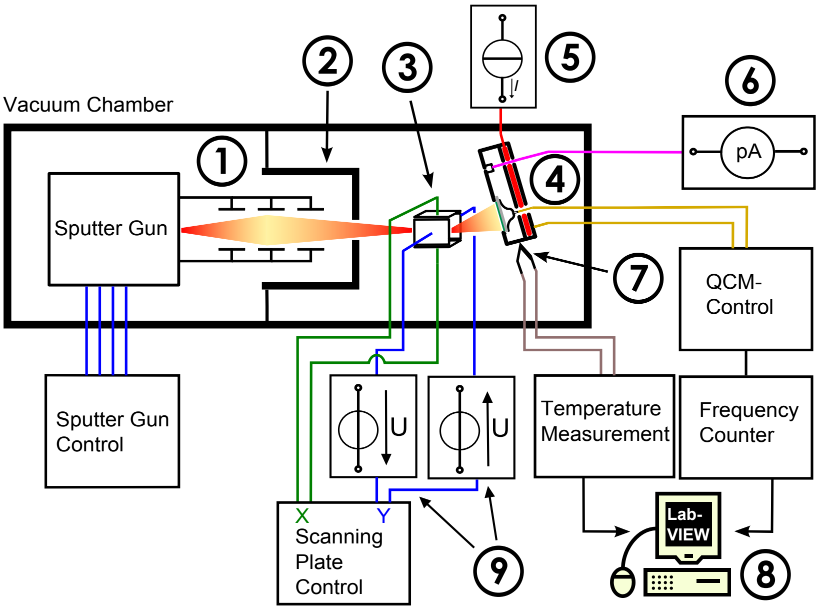

Figure 3.5 – measurement setup schematics without Wien velocity filter:

① ion source with einzel lens
② ∅ $5\,\mathrm{mm}$ aperture
③ scanning and deflection plate pairs
④ QCM holder with sample and FC
⑤ constant current supply for the QCM temperature control
⑥ picoampere meter to measure the ion current through the FC
⑦ thermocouple for QCM temperature measurements
⑧ PC with LabVIEW to log the QCM frequency and the temperature
⑨ additional voltage supplies to increase the $\vec{E}$-field strength of the deflection plates

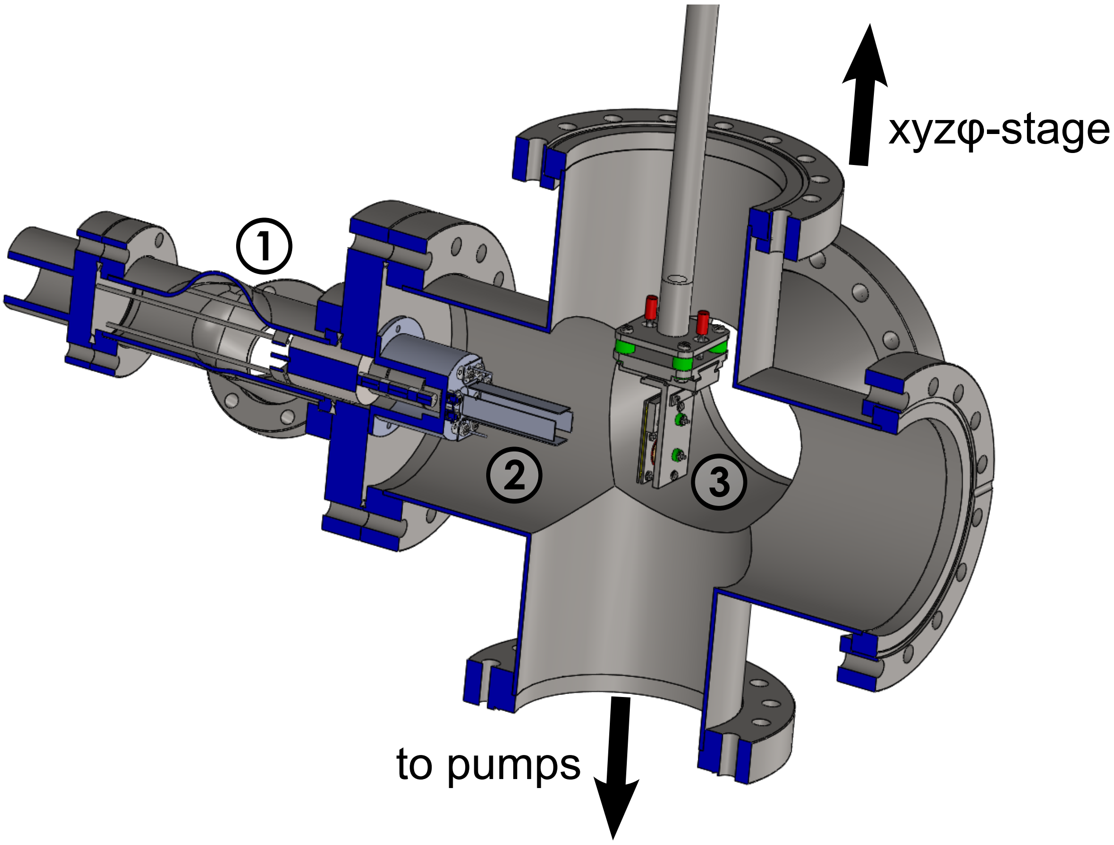

Figure 3.6 – sectional drawing of the measurement setup without Wien filter:
① sputter ion gun with an einzel lens
② Ø $5\,\mathrm{mm}$ hat-like aperture with deflection plates
③ QCM holder with Faraday cup. The position of the QCM holder can be adjusted with a xyzφ-stage.

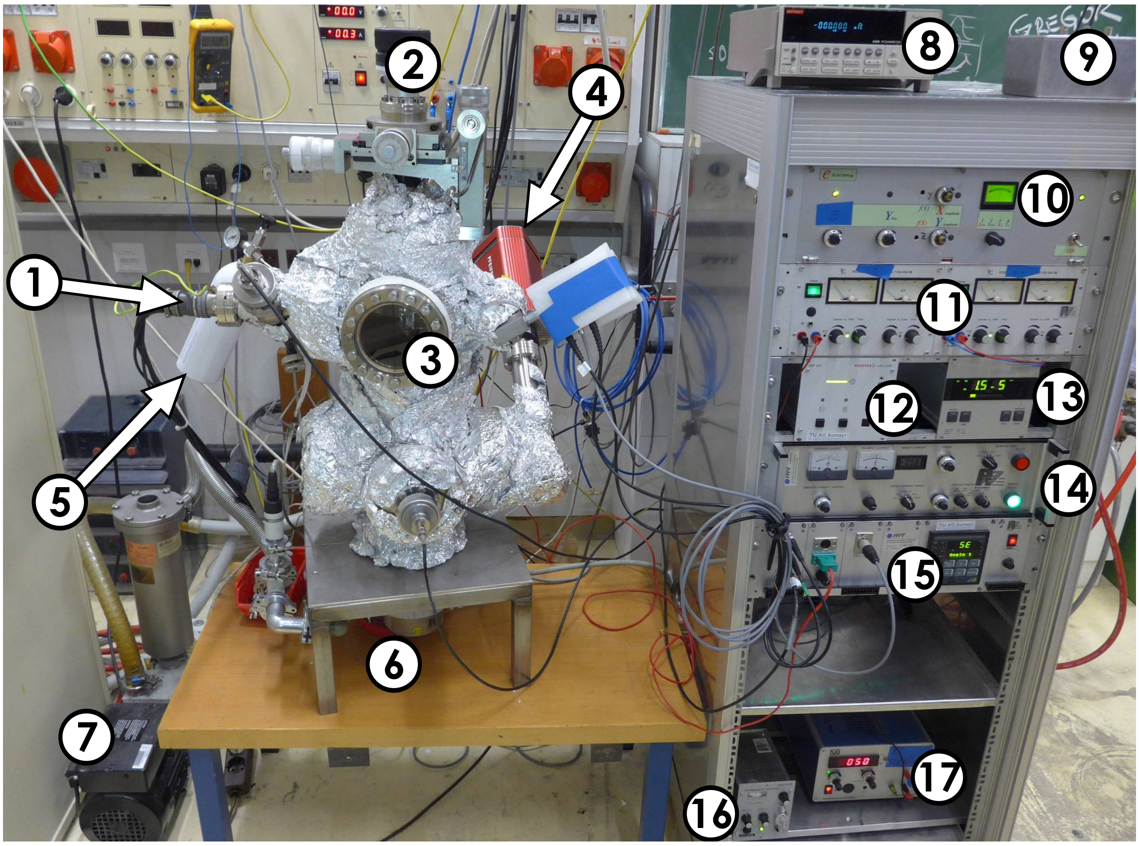

Figure 3.7 – photograph of the measurement setup:
① sputter ion gun connector
② xyzφ-stage
③ vacuum chamber containing the QCM holder with the FC, according to figure 3.5
④ quadrupole mass analyser
⑤ deuterium working gas bottle, connected to a gas dosing control valve
⑥ turbomolecular pump
⑦ pre vacuum pump
⑧ picoamperemeter to measure the ion current through the FC
⑨ battery pack of $+50\,\mathrm{V}$ to raise the potential of the FC (optional)
⑩ scanning plates control
⑪ 2 additional voltage supplies to increase the $\vec{E}$-field strength of the deflection plates
⑫ turbomolecular pump control
⑬ vacuum gauge controller
⑭ sputter ion gun control
⑮ QCM control with temperature measurement
⑯ gas dosing control valve control
⑰ voltage supply for FC secondary electron suppressor (optional)

3.2.1 Mass Spectra Measurements

The mass of D with $m = 2\,\mathrm{amu}$ is very low, therefore every heavier element in the gas source would cause a faulty increase of the resulting sputter yield. Without using a mass selected ion beam, a high purity working gas source is essential for accurate sputter yield measurements.

A quadrupole mass analyser is used to perform mass spectra measurements in the vacuum chamber. For these measurements the gas dosing device, controlling the deuterium gas supply, was set to the optimal working gas pressure of $1.3 \cdot 10^{-3}\,\mathrm{mbar}$ in the ion source. Ion current measurements showed the highest efficiency of the ion source at this pressure value. This working gas pressure causes an increase of the base pressure near the QCM to $1.6 \cdot 10^{-5}\,\mathrm{mbar}$.

Figure 3.8 shows a mass spectra, which was made after a baking time of the whole experiment of about 48 hours at 180 centigrade.

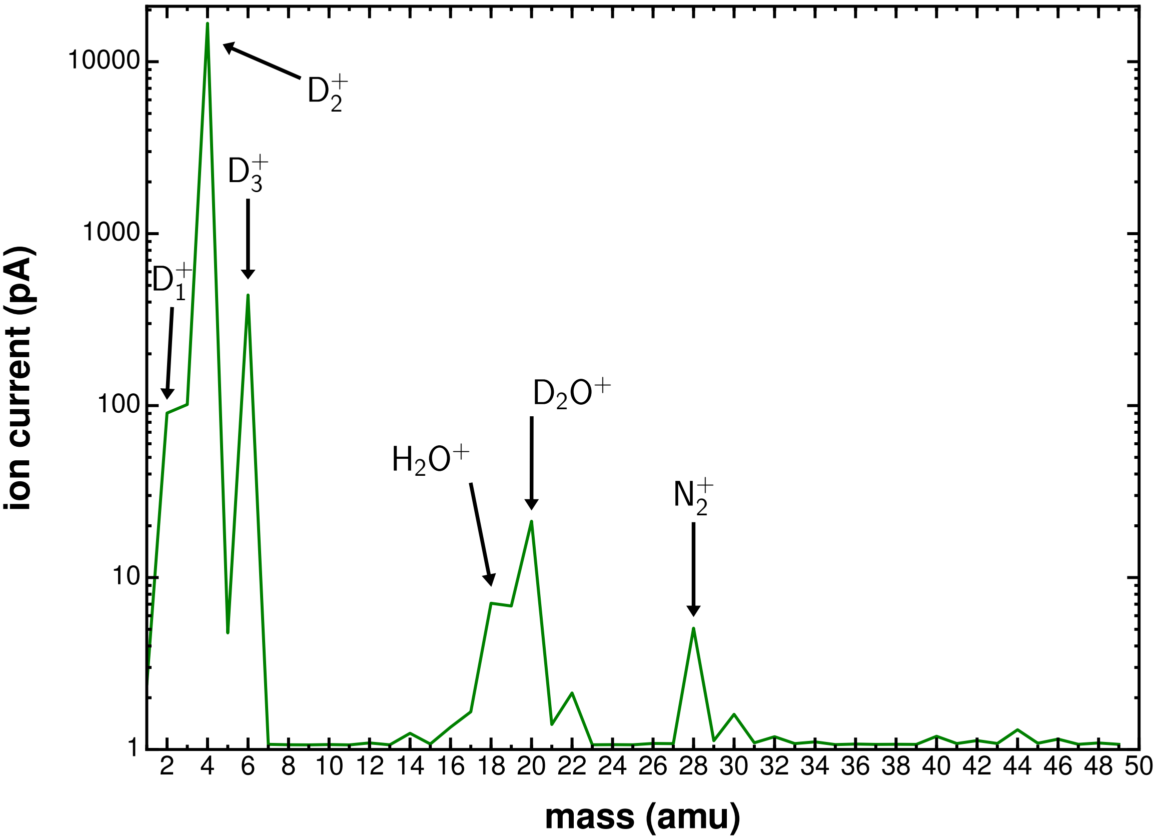

Figure 3.8 – Mass spectra, measured with a quadrupole mass analyser after 48 hours of baking. The main peaks are caused by deuterium, but also water and nitrogen were measured.

Table 3.3 – measured ion currents from figure 3.8, after 48 hours of baking.

mass [amu]	ion	current $[\mathrm{pA}]$	in %
2	D^+	89	0.51
4	D_2^+	16719	96.74
6	D_3^+	438	2.53
18	H_2O^+	6	0.03
19	HDO^+	6	0.03
20	D_2O^+	20	0.12
28	N_2^+	4	0.02
other	XY^+	3	<0.02

Table 3.3 shows the measured ion current of all relevant masses. The main ions are D, D_2 and the D_3 molecule, with a percentage of 99.8. Considerable heavier ions, like water and nitrogen occur only in an amount of $0.2\,\%$. The influence of these heavy ions to the sputter yield measurements should therefore be negligible small. Therefore sputter yield measurements with the setup without the Wien velocity filter are possible.

3.3 QCM Sample Holder

In this section the different QCM sample holder versions will be presented and discussed. The version number matches the year of manufacture.

3.3.1 Version 2011

Figure 3.9 shows a 3D CAD drawing of the 'old' QCM sample holder version 2011 and figure 3.10 a sectional drawing of it.

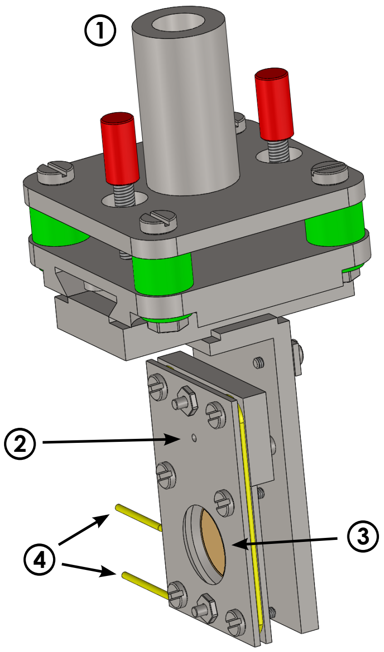

Figure 3.9 – 3D CAD drawing of the QCM holder version 2011:
① mounting kit for xyzφ stage
② FC aperture
③ QCM aperture
④ ohmic heating wires

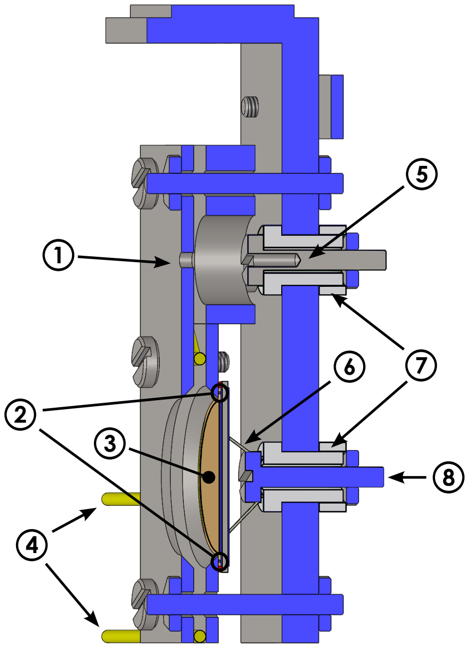

Figure 3.10 – sectional drawing of the QCM holder 2011
① FC aperture
② thin gold ring
③ QCM sample
④ ohmic heating wires
⑤ FC
⑥ tungsten spring
⑦ ceramic insulators
⑧ metal screw with tungsten spring as electrical connector for the crystal

The whole sample holder is mounted on a xyzφ stage, which allows exact positioning.
The quartz crystal sample is clamped between the top plate of the sample holder and a tungsten spring on the back plate. To improve the electric conductivity a thin gold ring is also clamped between the crystal and the front plate. The tungsten spring with a screw allows electrical connection to the QCM electronics. Ohmic heating wires allows operating the quartz crystal at its optimal operating temperature.
The sample holder includes also a FC, to measure the ion current. Doing so requires manipulating the FC via a xyzφ stage into the ion beam.
This sample holder works fine, but has some essential disadvantages:

- FC design: The diameter of the aperture is equal to the diameter of the FC hole and the distance between aperture and FC is about $4\,\mathrm{mm}$. An ion beam entering the aperture of the FC with a slight angular distribution hit the surface of the FC and will therefore not enter the hole. Electrons from secondary electron emission can easily exit the FC and will therefore falsify ion current measurements. By using a $+50\,\mathrm{V}$ battery pack between the picoampere meter and the FC, an attractive potential for electrons can be generated, which minimises loosing secondary electrons. On the other hand a perfectly shielded cable from the FC to the picoampere meter is essential, to avoid collecting electrons from everywhere else. This shielding is inside the vacuum chamber very difficult to achieve, especially at the contact point to the FC and at the chamber feed through. Therefore a redesign to a FC with a secondary electron suppressor plate would increase the accuracy of the ion current measurements.

- sample position: The quartz crystal sample is located $3\,\mathrm{mm}$ behind the front plate and is mounted behind a second plate, as can be seen in figure 3.10. Both plates have an aperture of the same size. This means a homogeneous ion bombardment of the quartz sample surface is only possible at normal incidence, while any other angle of incidence causes a shadowing effect. For small angles of impact ($\leq 5^\circ$) this effect is negligible, because the most sensitive region of the quartz sample is in its center [5,19]. Nevertheless angular dependent sputter yield measurements of steeper angles are not possible.

These disadvantages lead to a redesign of this QCM sample holder.

3.3.2 Version 2014, 2015

Figure 3.11 shows a 3D CAD drawing of the 'new' QCM sample holder version 2015 and figure 3.12 a sectional drawing of it.

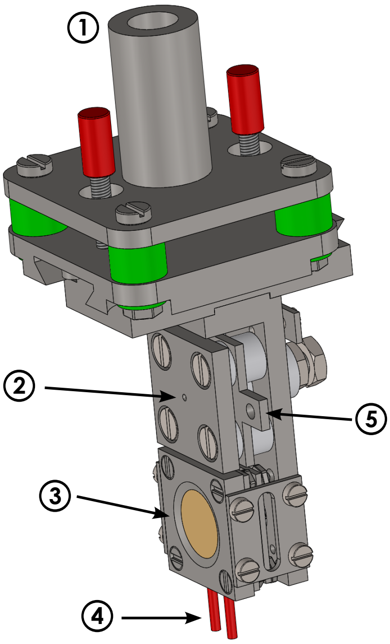

Figure 3.11 – 3D CAD drawing of the QCM holder version 2015:
① mounting kit for xyzφ stage
② FC aperture
③ front plate with QCM aperture
④ ohmic heating wires
⑤ electron suppressor aperture

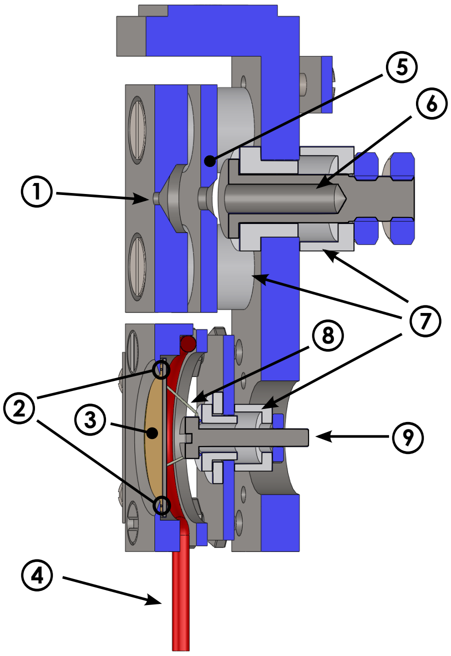

Figure 3.12 – sectional drawing of the QCM holder 2015
① FC aperture
② thin gold ring
③ QCM sample
④ ohmic heating wires
⑤ electron suppressor aperture
⑥ FC
⑦ ceramic insulators
⑧ tungsten spring
⑨ metal screw with tungsten spring as electrical connector for the crystal

In this version the front plate is separated into two regions. The upper one is the FC aperture, while the lower one is the front plate for the QCM. The quartz crystal is clamped between the front plate and a tungsten spring on the back, but due to a mechanical guiding in the front plate, the positioning of the quartz crystal is here much easier, compared to version 2011. To improve the electric conductivity a thin gold ring is also clamped between the crystal and the front plate. The design of the front plate allows ion beam incident angels

of up to 70 degrees, without risking a non uniform ion bombardment of the quartz crystal surface.
This design includes a secondary electron suppressor plate, which decreases the possibility of falsified ion current measurements, due to the escape of secondary electrons.
The prototype version 2014 was designed by B.M. Berger and is nearly equal to version 2015. In version 2015 the FC was improved, by increasing its size and the drill hole. Because of that every ion passing the FC aperture and the suppressor aperture will enter the FC hole and cannot hit the front end of the FC any more.

3.4 General Sputteryield Measuring Process

To evaluate the mass removal rate of a sample by using the QCM technique, two measurements are essential: measuring the ion current density and the QCM resonance frequency over time under ion bombardment, as described in chapter 2.3.
The ion current cannot be measured during the ion bombardment of the sample, therefore it is done before and after it. Both ion current measurements were averaged and used for the sputter yield calculation. The measuring steps are described in detail hereinafter:

Ion current density measurement: At first the QCM holder is brought into position via the xyzφ-stage, so that the distance between the FC and the neutral beam axis is $9\,\mathrm{mm}$, according to figure 3.3. After activating the ion source, by applying an appropriate acceleration voltage, the deflection plates are adjusted, to bend the ion beam into the FC. After fine tuning the ion source to maximize the ion current, beam scanning is activated and properly adjusted. This is necessary to cover an area equal to the area of the quartz crystal with a uniform ion current density. The resulting beam profile is checked by moving the FC in steps of $1\,\mathrm{mm}$ in both transverse directions of the ion beam, to $\pm 3\,\mathrm{mm}$. Variations in the current density are kept below 10% to achieve a constant areal mass change of the quartz sample.

Measurement of the QCM resonance frequency over time: After finishing the ion current density measurement, the ion source is deactivated by switching off its acceleration voltage. Afterwards the quartz crystal sample is brought into the ion beam path, using the xyzφ-stage.
The QCM control is permanently active to avoid falsify frequency measurements, caused by electronics warming. It forwards continuously the actual resonance frequency to a frequency counter, which is connected to the measuring PC. As soon as the LabVIEW data logging software on the measuring PC is executed, the QCM measurement starts. It logs the frequency of the crystal, the temperature of the QCM sample holder and the working gas pressure of the sputter gun in an ASCII text file, with a 1 second sample rate.
A delay time of about 200 seconds is used to log the behaviour of the quartz crystal without

mass change. After that the ion source is reactivated and the ion bombardment of the sample starts. Figure 3.13 shows a sketch of such a measurement.
The sputter gun is deactivated again, after an appropriate ion bombardment time, and after another delay time of about 200 seconds, the data logging is stopped.

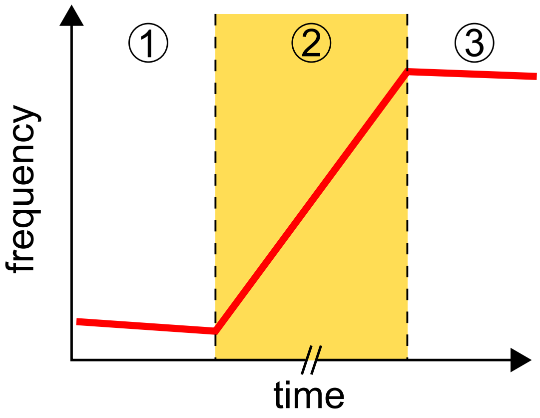

Figure 3.13 – Sketch of a QCM measurement.
This figure shows the resonance frequency of the QCM over time. The sample ion bombradment occurs during phase ②. During the phases ① and ③ the ion source is switched off. The slope of the signal in phase ② gives information of the mass change of the sample, while the slopes in phase ① and ③ can be used to evaluate the quartz drift.

Data Analysis: As soon as the ion current density measurement is repeated, the sputter yield can be calculated. All relevant measurement parameters, like target film material(s), projectile element, ion energy, degree of ionisation, ion current distribution before and after the bombardment, start/stop times, parameters for deflection plate pair, log-data filename, heating current through the quartz crystal heating, QCM holder informations and ion source settings are stored in an Excel-file.
Both files can be opened and analysed via a PYTHON program, developed and programmed during this thesis. It offers several functions for filtering and plotting the measured data in different ways and to calculate resulting sputter yields.

3.5 Error Estimation and Propagation

As discussed in the last chapter, two measurements are essential to evaluate the sputter yield. The mass change of the QCM and the projectile particle flux (equation 2.3.2). Precise knowledge of the ion current and the time derivative of the resonance frequency of the QCM are therefore very important. Both measurements are affected by uncertainties which will be discussed here:

Following notation will be used in this chapter:

X measured value
$\bar{X}$ average value (arithmetic mean)
ΔX error of measured value
$\sigma_X = \frac{\Delta X}{X}$ relative error
$\dot{X} = \frac{\Delta X}{\Delta t}$ time derivative

The standard deviation and the average value are calculated according to following equations:

$$\Delta X_{STD} = \sqrt{\frac{1}{n-1}\sum_{i=1}^{n}\left(X_i - \bar{X}\right)^2} \qquad \text{with} \qquad \bar{X} = \frac{1}{n}\sum_{i=1}^{n} X_i$$

3.5.1 Ion Current Density

The ion current I is measured with an FC at different positions, to analyse the ion beam profile, as described in chapter 3.4. This measurement gives seven ion current values in both transverse directions. These values were averaged in every direction, which gives $\bar{I}_H$ and $\bar{I}_V$ for the horizontal and vertical ion current. As error the standard deviation is calculated for both direction, which gives ΔI_H and ΔI_V. The following relative errors $\sigma_{I_V} = \Delta I_V / \bar{I}_V$ and σ_{I_H} are excellent values to check the quality of the beam scanning and were kept below $10\,\%$.

The ion beam profile measurements are combined, by averaging the horizontal and vertical ion current values. The resulting error value follows from the Gaussian error propagation theorem:

$$\begin{aligned} \bar{I}_{bevore}, \bar{I}_{after} &= 1/2 \cdot (\bar{I}_V + \bar{I}_H) \\ \Delta I_{bevore}, \Delta I_{after} &= 1/2 \cdot \sqrt{\Delta I_V{}^2 + \Delta I_H{}^2} \end{aligned} \tag{3.5.1}$$

As described in chapter 3.4, an ion beam profile measurement is done before and after the ion bombardment of the sample. The ion current density is assumed to be constant during the sample bombardment, but changes due to variations of temperature, working gas pressure or the filament current of the ion source are hard to avoid and need to be included in the

error calculations:
The total ion current for sputter yield calculations follows from averaging the ion current before and after the sample bombardment:

$$I_{total} = 1/2 \cdot (\bar{I}_{before} + \bar{I}_{after}) \tag{3.5.2}$$

A maximum error estimation is done for the total ion current. It includes deviations between the ion current measurement before and after the sample bombardment, by adding the difference of both measurements to the error and also the error resulting from imperfections of the ion beam profile:

$$\Delta I_{total} = |\bar{I}_{before} - \bar{I}_{after}| + \Delta I_{scan} \qquad \text{with} \qquad \Delta I_{scan} = 1/2 \cdot (\Delta I_{before} + \Delta I_{after}) \tag{3.5.3}$$

The ion current density follows by normalizing the ion current, using the area A_{FC} of the FC aperture:

$$j = \frac{I_{total}}{A_{FC}} \tag{3.5.4}$$

An accurate knowledge of the size A_{FC} of the FCs ion entrance aperture is therefore important too and will be discussed in the next section.
According to the Gaussian error propagation theorem, the relative error of the ion current density is simply:

$$\sigma_j = \sqrt{\sigma_I^2 + \sigma_{A_{FC}}^2} \tag{3.5.5}$$

3.5.1.1 Faraday Cup Aperture Measurements

Although the drilling of the FC aperture holes were very well performed, the real size of the drillings were cross-checked with a confocal 3D microscope (Type nanofocus μsurf explorer). Figure 3.14 shows some images of these measurements for the different types of sample holder versions.

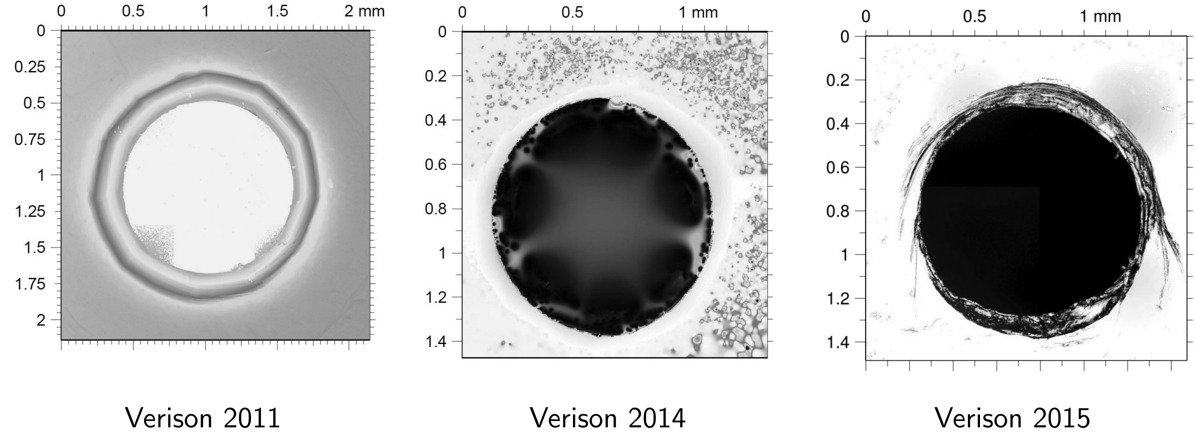

Figure 3.14 – Images of the FC apertures, using a confocal microscope. Some imperfection in drilling lead to slight elliptic holes and some edges in the apertures.

The microscope measurements were performed a couple of times for each sample holder version. Using these images and the software 'ImageJ' (Version 1.48v[1]) the resulting area of the FC apertures were calculated and can be seen in table 3.4.

Table 3.4 – Resulting FC aperture areas from the confocal microscope images

QCM holder Version	measured area $[\mathrm{mm}^2]$	relative error [%]
2011	1.113	2.8
2014	0.849	0.8
2015	0.970	3.3

The number of measurements for each aperture version is with 2 to 4 very low, therefore these calculated errors are an estimation only.

For error propagation calculations the relative error was rounded up, to be on the safe side and equally set for every FC aperture version to:

$$\boldsymbol{\sigma_{A_{FC}} = 3.5\,\%} \tag{3.5.6}$$

3.5.2 Resonance Frequency

The resonance frequency of the crystal is on the one hand dependent on its own mass plus the deposited material mass (compare chapter 2.3), but on the other hand on some unwanted parameters, like temperature, residual gas pressure and the 'natural' ageing of the

---

[1] `http://imagej.nih.gov/ij/` last access: 10.12.2015

crystal [5]. Luckily sputter yield calculations require the time derivative of the resonance frequency $\dot{f} = \frac{\Delta f}{\Delta t}$, so as long as the unwanted parameters are constant, they do not need to be taken into account.

3.5.2.1 Error propagation with quartz drift

Figure 3.13 shows a sketch of a simplified QCM measurement. The frequency signal is linearly fitted in every phase, using a least-squares regression algorithm. The slope of the signal during the 'beam off' phases $\dot{f}_1$ and $\dot{f}_3$ can give information about the quartz drift, while the slope of the 'beam on' phase $\dot{f}_2$ gives the information about the mass change of the sample.
To include the quartz drift in the sputter yield calculations, the slopes of the 'beam off' phases were averaged and subtracted from the slope during the 'beam on' phase:

$$\dot{f} = \dot{f}_2 - \dot{f}_{drift} \qquad \text{whith} \qquad \dot{f}_{drift} = 1/2 \cdot (\dot{f}_1 + \dot{f}_3) \tag{3.5.7}$$

The algorithm calculates also the uncertainties $\Delta\dot{f}$ for every linear fit phase. These error are included according to the Gaussian error propagation law:

$$\Delta\dot{f}_{fit} = \sqrt{\Delta\dot{f}_2^2 + 1/4 \cdot (\Delta\dot{f}_1^2 + \Delta\dot{f}_3^2)} \tag{3.5.8}$$

A maximum error estimation is done for evaluating the error of the total frequency change. It includes deviations between the quartz drift before and after the sample bombardment, by adding the difference of both measurements to the error and also the linear fit errors:

$$\Delta\dot{f} = |\dot{f}_3 - \dot{f}_1| + \Delta\dot{f}_{fit} \tag{3.5.9}$$

3.5.2.2 Error propagation without quartz drift

In comparison to the simplified QCM measurement from figure 3.13, high flux measurements show a couple of transient effects between the beam off and on phases:

- Due to the high ion flux from the new experimental setup, a warming of the quartz crystal of up to 10 centigrade can occur, after activating the ion beam and a cooling of it, after deactivating.

- The base pressure in the vacuum chamber under measuring conditions is with $1 \cdot 10^{-5}\,\mathrm{mbar}$ quite high. Up to 10 monolayers per second of adsorbates may be deposited on the sample, as soon as the ion beam is switched off and cause an additional mass change of the sample.

These temperature variations and the mass increase of the sample due to adsorbates causes resonance frequency changes and are much stronger than the natural quartz drift of some mHz [5, 19]. Therefore the quartz drift is negligible and not included to high flux sputter yield calculations.
Consequential the slope of the signal during the beam on phase is used for the calculations only:

$$\dot{f} = \dot{f}_2 \qquad \text{and} \qquad \Delta\dot{f} = \Delta\dot{f}_2 \tag{3.5.10}$$

3.5.3 Sputter Yield Error

As discussed in the beginning of this chapter, the sputter yield depends on two main parameters: The ion current density j and the frequency change $\dot{f} = \frac{\Delta f}{\Delta t}$. For the resulting sputter yield relative error σ_y, the maximum error as sum of all relative errors is used plus an error caused by impurities in the ion beam:

$$\sigma_y = \sigma_j + \sigma_{\dot{f}} + \sigma_{impure} \tag{3.5.11}$$

The error σ_{impure} can be estimated using the residual gas mass spectre from figure 3.8. About $0.2\,\%$ of impurities, like water and nitrogen were measured.
Assuming all of these impurities have the same sputteryield as pure nitrogen and doing the same estimation as in chapter 3.1.1, by assuming an ion beam with $0.2\,\%$ nitrogen and $99.8\,\%$ deuterium, the combined sputter yield Y_{DNW} can be estimated as the weighted average of both single ion sputter yields:

$$\frac{Y_{DW} \cdot 0.998 + Y_{NW} \cdot 0.002}{Y_{DW}} = 104.8\,\% \tag{3.5.12}$$

where Y_{DW} is the sputteryield of deuterium bombarding pure tungsten at $1000\,\mathrm{eV}$ and Y_{NW} the sputteryield of nitrogen on tungsten.
The resulting sputter yield is about 5% higher and therefore the impurity error is estimated to:

$$\boldsymbol{\sigma_{impure} = 5\,\%} \tag{3.5.13}$$

3.6 Sputtering of W by D Comparison Measurment

Comparison measurements were performed, to test the new setup. Only experiments with $D_2{}^+$ will be reported here and results are given per D-atom. For these measurements a quartz crystal sample with a pure tungsten film was used and bombarded with D ions at an energy of $1000\,\mathrm{eV/D}$. At first a measurement was performed using the 'old' experimental setup with the existing ECR ion source SOPHIE. Afterwards the same measurements were performed, using the new setup with the sputter ion gun and different QCM sample holder versions.

The results can be seen in figure 3.15, 3.16 and 3.17.

Table 3.5 compares these measurements among each other and figure 4.2 compares the resulting D on W sputter-yield with data from literature.

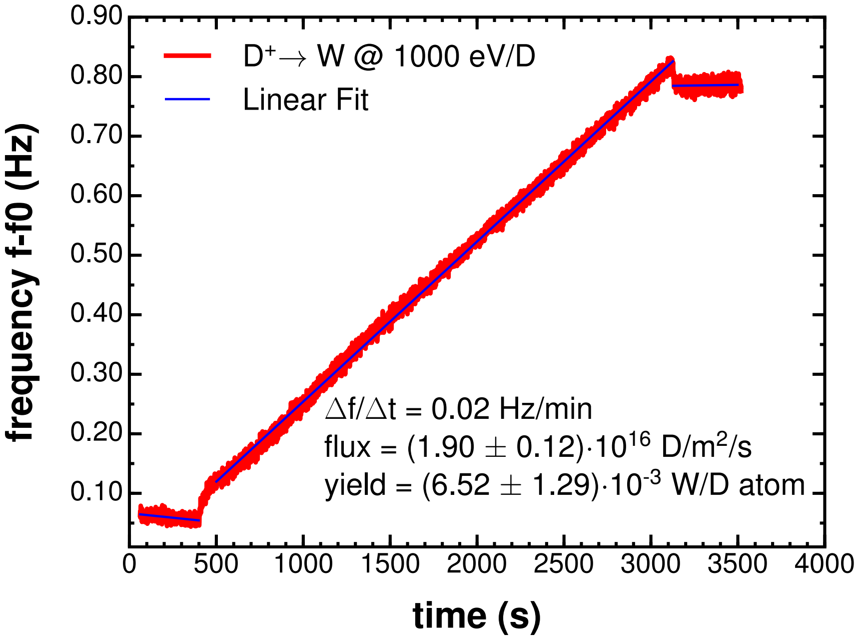

Figure 3.15 – D → W sputter yield measurement using the ion source SOPHIE and QCM holder version 2014. The deuterium ion beam was active from $t = 400\,\mathrm{s}$ to $t = 3100\,\mathrm{s}$ and provided an ion current density of $j = (152.1 \pm 9.8)\,\mathrm{nA/cm^2}$.

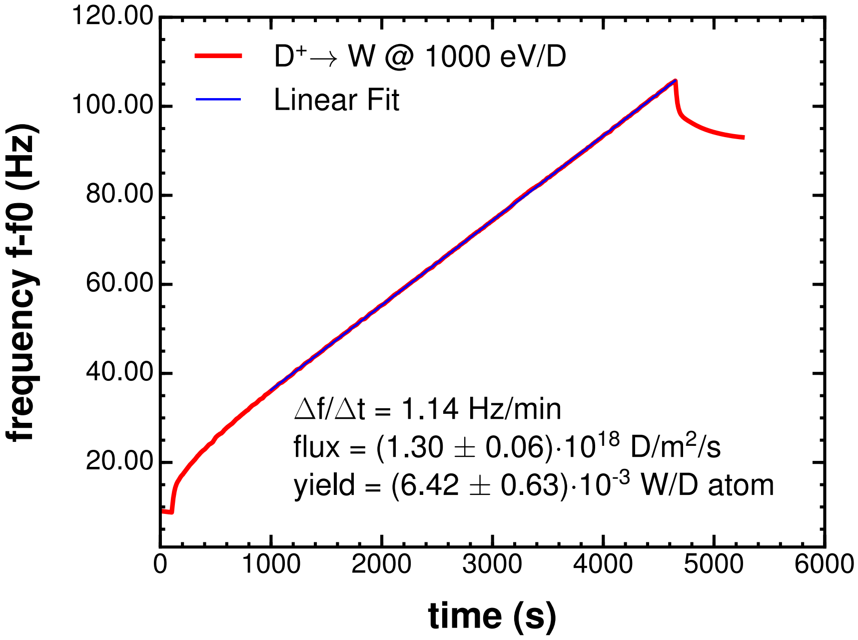

Figure 3.16 – D → W sputter yield measurement, using the new experimental setup with QCM holder version 2011. The deuterium ion beam was active from $t = 100\,\mathrm{s}$ to $t = 4650\,\mathrm{s}$ and provided an ion current density of $j = (10.45 \pm 0.49)\,\mu\mathrm{A/cm}^2$.

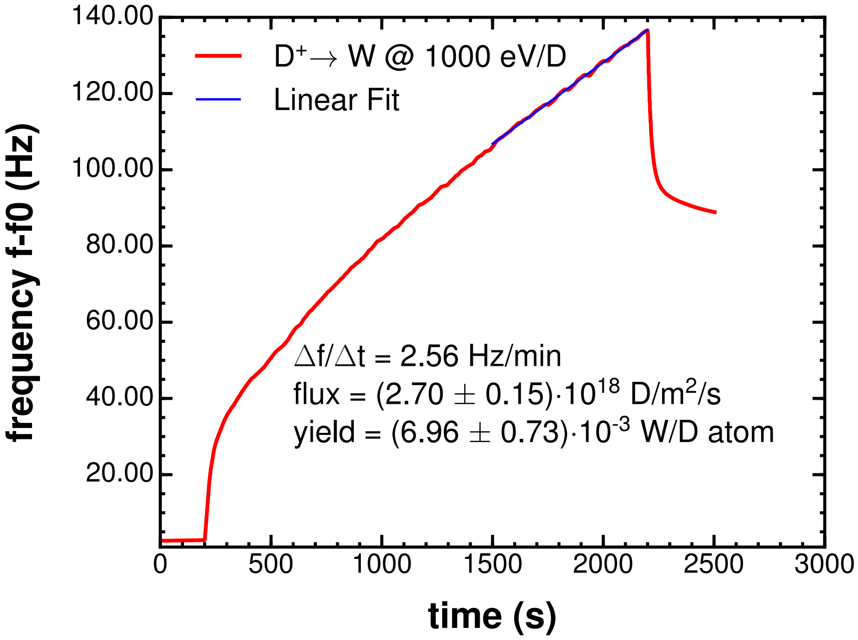

Figure 3.17 – D → W sputter yield measurement using the new experimental setup with QCM holder version 2015. The deuterium ion beam was active from $t = 200\,\mathrm{s}$ to $t = 2200\,\mathrm{s}$ and delivered an ion current density of $j = (21.59 \pm 1.16)\,\mu\mathrm{A/cm}^2$.

Table 3.5 – D → W sputter yields measurement results at $1000\,\mathrm{eV/D}$, using different setup constellations

ion source	QCM holder version	ion flux $[\cdot 10^{16}\,\mathrm{D/m^2/s}]$	sputter yield $[\cdot 10^{-3}\,\mathrm{W/D}]$
SOPHIE	2014	1.90 ± 0.12	6.52 ± 1.29
sputter ion gun	2011	130 ± 6	6.42 ± 0.63
sputter ion gun	2015	270 ± 15	6.96 ± 0.73

3.6.1 Discussion

The frequency response of the QCM is not instantly linear after activating the ion beam. This behaviour is caused by local heating and stress of the sample due to the ion bombardment and takes some time until equilibrium is reached. The same effect can be seen after deactivating the ion beam, but the other way round. Due to the higher ion flux of the new setup, this effect is very strong here and needs to be taken into account for measuring the slope of the frequency change. Therefore the linear fitting of the signal starts with a certain delay, as can be seen in figure 3.16 and 3.17.

Adsorbats play a certain role too. The working gas pressure in the sputter ion gun of $1.3 \cdot 10^{-3}\,\mathrm{mbar}$ causes an increase of the base pressure near the QCM from $\approx 10^{-9}\,\mathrm{mbar}$ to $1.6 \cdot 10^{-5}\,\mathrm{mbar}$. At this pressure and assuming a sticking coefficient of 1, approximately 10 monolayers of adsorbats deposit on the sample per second. This can be seen as a drop in the resonance frequency after switching off the ion beam, but the adsorbats are also removed quickly as soon as the ion beam is active again. This pressure is however comparable to the interior of a working fusion reactor.

Table 3.5 lists the resulting D → W sputter yields, measured with every setup constellations. Although the final values differ slightly, every setup delivers useful results. The significantly higher error with SOPHIE is caused by the low signal to noise ratio, because of the low deuterium ion flux and also the very low sputter yield of tungsten by deuterium bombardment in general.

Comparing the ion flux of both experiments show another important result: the measured flux using the new setup, is $2.7 \cdot 10^{18}\,\mathrm{D/m^2/s}$ and about a factor of 140 higher than the flux reached with SOPHIE, of $1.9 \cdot 10^{16}\,\mathrm{D/m^2/s}$. This means that reaching a fluence of $1 \cdot 10^{23}\,\mathrm{D/m^2}$ will take only about 11 hours, instead of 100 days, which makes high fluence measurements possible.

4 Transient Effects during Sputtering of WN by D

In this chapter sputter yield measurements of pure W targets, as well as the evolution of the fluence dependent mass removal rate of WN targets are presented and discussed.
The first part describes the preparation of the samples. The second part presents sputter yield measurements on pure W targets and different projectile energies and compares them to data from literature. The third part presents high fluence measurements of WN targets with a WN = 1:1 concentration ratio, at projectile energies of $250\,\mathrm{eV/D}$, $750\,\mathrm{eV/D}$ and $1000\,\mathrm{eV/D}$.

4.1 Preparation of W an WN Samples

Different techniques are used to deposit the sample material on the quartz crystals. Figure 4.1 shows the used sample preparation holder, which is brought into the material deposition chambers. It ensures that the sample material deposits on the right place onto the quartz crystals and is also a mechanical protection of the crystals.

The pure W samples were prepared at the thin film group of the institute of solid state physics at TU Wien, by C. Eisenmenger-Sittner. A magnetron sputter deposition device (Type ALCATEL/ADIXEN SCM 451) was used to deposit a polycrystalline tungsten film of about $300\,\mathrm{nm}$ on top of one electrode of the virgin quartz crystals.

The WN samples were prepared at the Jožef Stefan Institute in Ljubljana, Slovenia, by M. Čekada. A triode sputter apparatus (Type Balzer Sputron) was used to deposit WN films on one side of the electrodes of the virgin quartz crystals, with a composition ratio of $50\ at.\%$ W and $50\ at.\%$ N and a layer thickness of about $360\,\mathrm{nm}$. To improve the adhesion of this layer, a $20\,\mathrm{nm}$ chromium (Cr) and a $10\,\mathrm{nm}$ pure W interlayer was deposited first. The resulting composition was checked by using the Time-of-Flight Elastic-Recoil-Detection-Analysis (TOF-ERDA) technique (for details of this technique see [42]). The 1:1 WN composition concentration could be confirmed, but also impurities of about $5\ at.\%$ O and $3\ at.\%$ Ar have been measured [22].

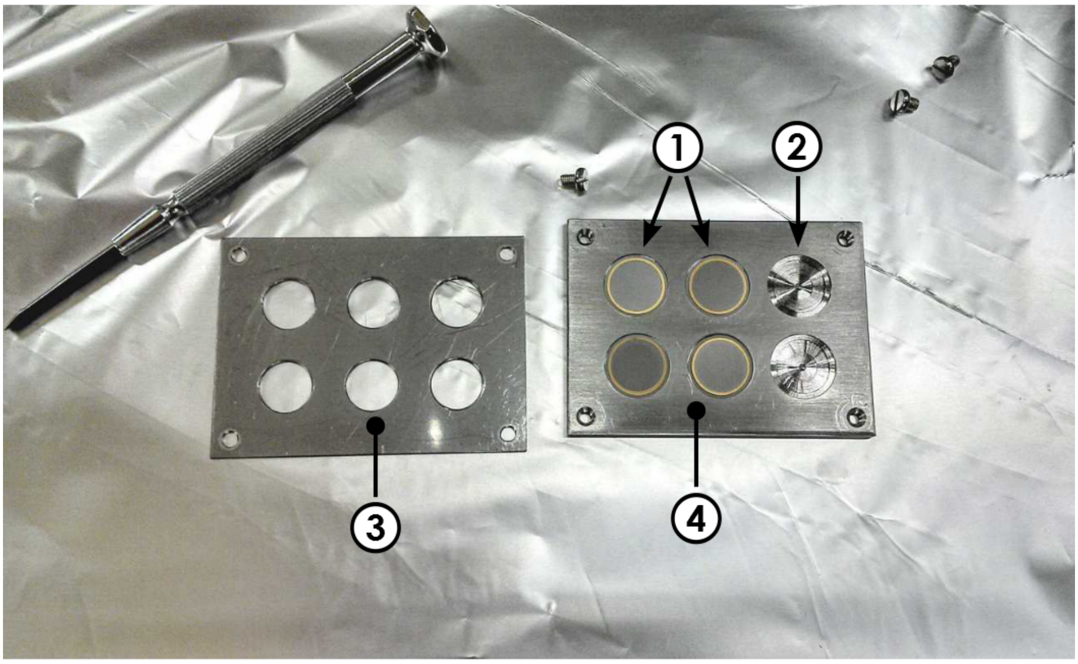

Figure 4.1 – Disassembled sample preparation holder, to allow deposition of sample material on top of one of the gold electrodes of each quartz crystal. The base plate ④ offers six spots for the quartz crystals. A top mask ③ ensures, that the edge of the crystals electrode stays undeposited, to allow electrical conductivity afterwards. The picture shows four already deposited quartz crystals ① and two free spots ②.

4.2 Sputtering of W by D

As a pre step for investigating WN samples, sputter yields of pure W samples at different energies were measured. One the one side this is necessary to test the experimental setup, by comparing the results with data from literature and on the other side to be able to compare the sputtering behaviour of pure W with WN targets.
Table 4.1 shows the measured results and figure 4.2 compares these results with data from literature.

Table 4.1 – D → W sputter yields measurement results at different ion energies

ion energy $[\mathrm{eV/D}]$	mass removal rate $[\mathrm{amu/D}]$	sputter yield $[\cdot 10^{-3}\,\mathrm{W/D}]$
500	0.52 ± 0.05	2.8 ± 0.3
750	0.85 ± 0.15	4.6 ± 0.8
1000	1.19 ± 0.15	6.6 ± 0.5

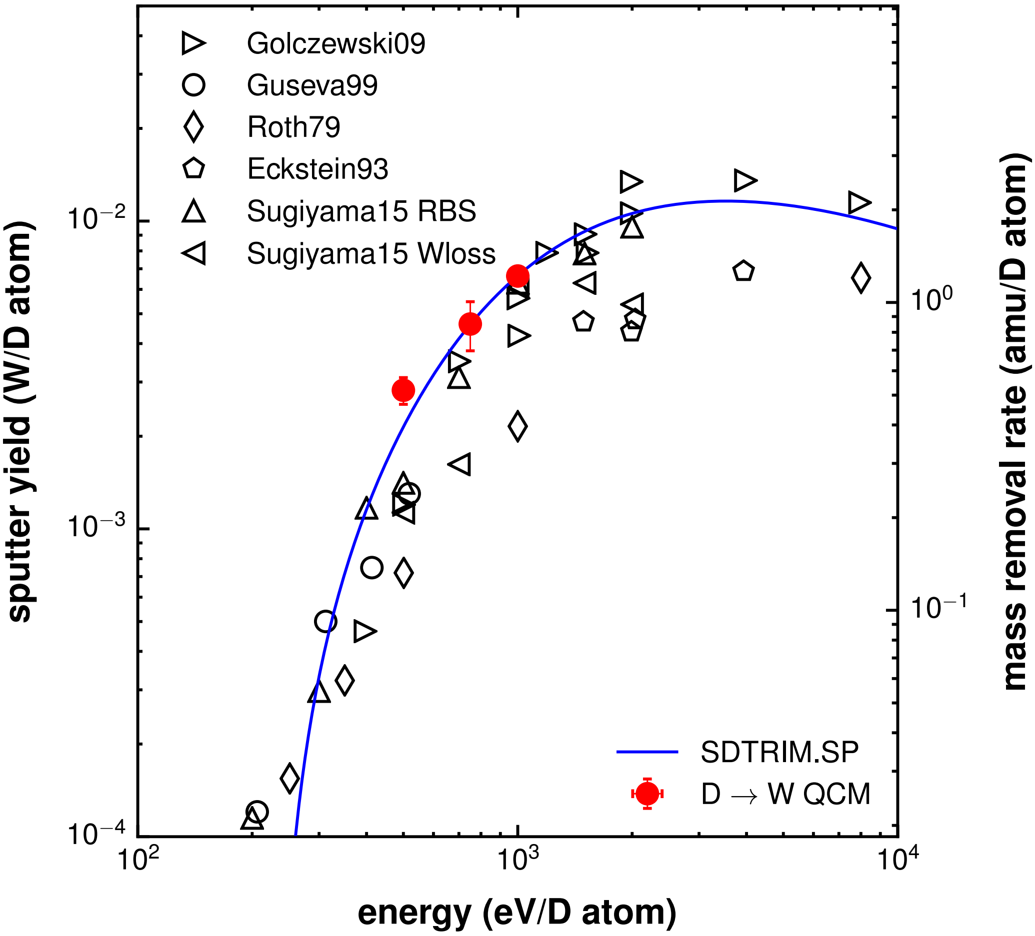

Figure 4.2 – D → W sputter yield measurements at different energies in comparison to other experiments from literature [30, 43, 44]. The solid blue line represents an SDTRIM.SP numeric simulation.

Data from literature and other measurements vary widely. Nevertheless our QCM measurement results are plausible, as can be seen in figure 4.2. Dynamic sputtering calculations with SDTRIM.SP agree very well with the QCM measurements.
Measurements at ion energies of $250\,\mathrm{eV/D}$ were unfortunately not possible, because the mass change and therefore the frequency change of the QCM is too low and in the range of the quartz drift, which makes accurate sputter yield measurements impossible.

4.3 Sputtering of WN by D

To investigate the D fluence dependent evolution of the mass removal rate of WN and W targets, measurements were performed at D ion energies of $1000\,\mathrm{eV/D}$, $750\,\mathrm{eV/D}$ and $500\,\mathrm{eV/D}$. Figure 4.3 shows the fluence dependent mass removal rate at $1000\,\mathrm{eV/D}$ and figure 4.4 at $500\,\mathrm{eV/D}$.

Due to the limited amount of samples, the measurement at $750\,\mathrm{eV/D}$ was performed after the $1000\,\mathrm{eV/D}$ measurement, using the same quartz crystal sample. This means that the $750\,\mathrm{eV/D}$ measurement started with a WN concentration different to 1:1 and therefore only the steady state sputter yield could be evaluated and no relevant transient effects could be investigated. In table 4.2 the resulting steady state mass removal rates at different energies are presented.

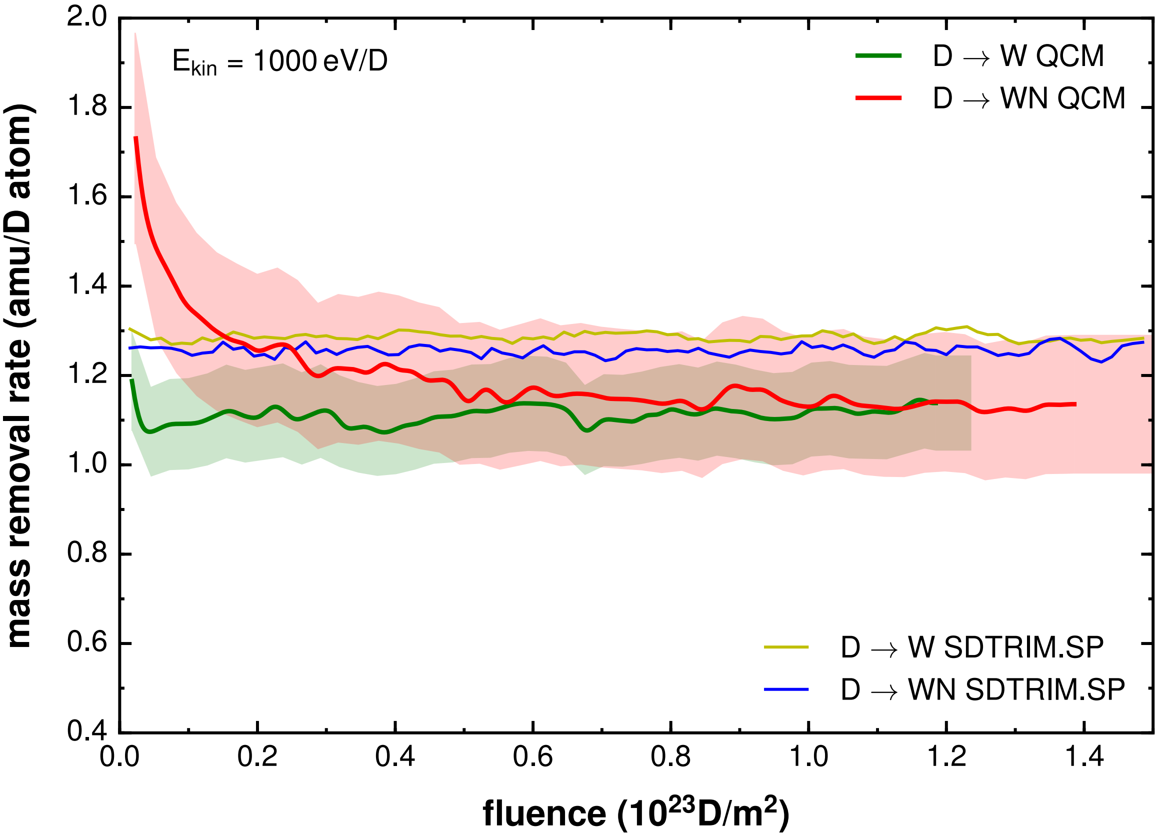

Figure 4.3 – D → W and WN fluence dependent mass removal rate QCM measurements at a kinetic projectile energy of $1000\,\mathrm{eV/D}$ and an ion flux of $1.5 \cdot 10^{18}\,\mathrm{D/m^2/s}$. The mass removal rate of the pure W target is nearly constant, while the WN target shows a fluence dependent decrease. After a fluence of about $0.6 \cdot 10^{23}\,\mathrm{D/m^2}$ the mass removal rates of both measurements are equal. The light red and light green areas represent the possible error. Dynamic sputtering calculations with SDTRIM.SP reproduce the steady state mass removal rates very well, but a fluence dependent transient effect of the mass removal rate cannot be seen here.

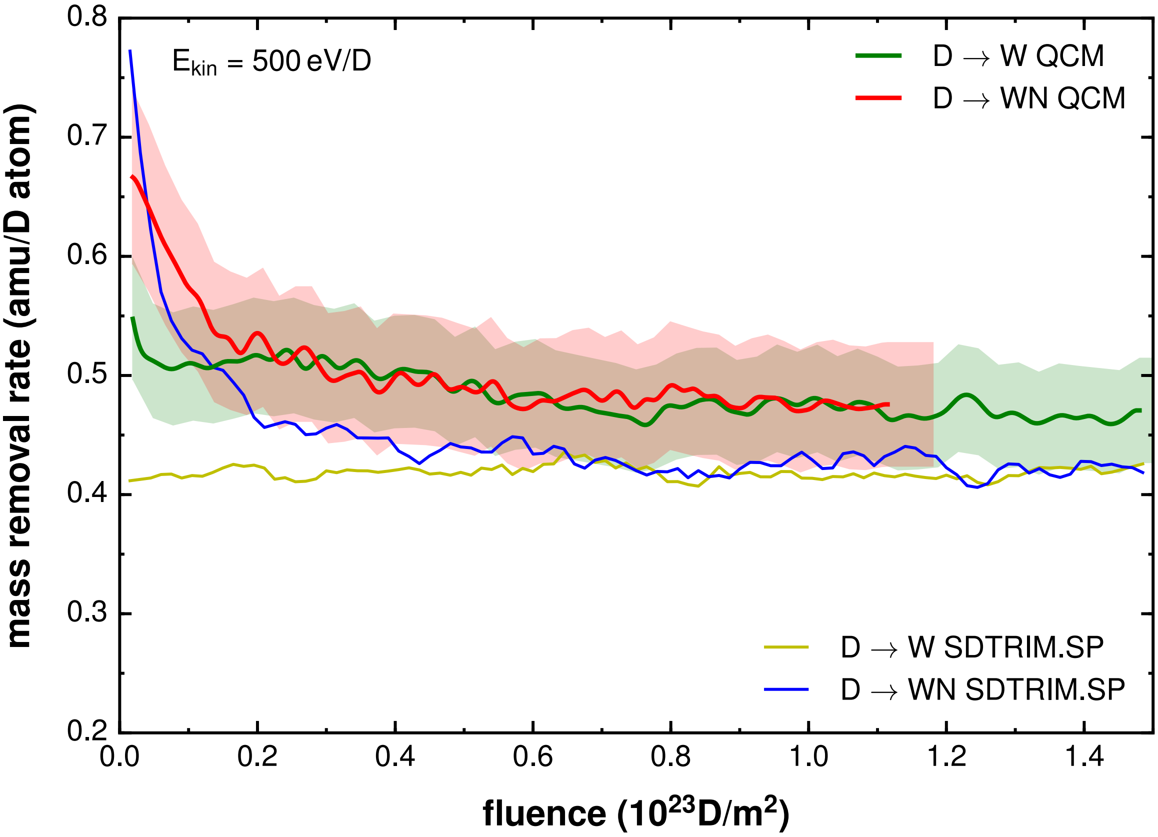

Figure 4.4 – D → W and WN fluence dependent mass removal rate QCM measurements at a kinetic projectile energy of $500\,\mathrm{eV/D}$ and an ion flux of $1.4 \cdot 10^{18}\,\mathrm{D/m^2/s}$. The mass removal rate of the pure W target is nearly constant, while the WN target needs a fluence of about $0.2 \cdot 10^{23}\,\mathrm{D/m^2}$ to reach the same value, as of pure W. The light red and light green areas represent the possible error. Dynamic sputtering calculations with SDTRIM.SP predict a slightly lower mass removal rate, but is still at the lower border of the error areas. The simulation with the WN target shows also a drop in the mass removal rate at low fluences.

Table 4.2 – D → WN mass removal rate measurement results at different ion energies, after reaching steady state conditions:

ion energy $[\mathrm{eV/D}]$	mass removal rate $[\mathrm{amu/D}]$
500	0.48 ± 0.05
750	0.77 ± 0.07
1000	1.14 ± 0.16

Both high fluence measurements show transient effects of the mass removal rate during bombardment of the WN targets. At $1000\,\mathrm{eV/D}$ (figure 4.3) the mass removal rate decreases from about $1.7\,\mathrm{amu/D}$ to the same value as of pure W, of about $1.1\,\mathrm{amu/D}$. A fluence of $0.6 \cdot 10^{23}\,\mathrm{D/m^2}$ is necessary for that. The measurement at $500\,\mathrm{eV/D}$ (figure 4.4) shows a similar transient effect, but the required fluence is lower. Here a fluence of about $0.2 \cdot 10^{23}\,\mathrm{D/m^2}$ is necessary that the mass removal rate drops from about $0.65\,\mathrm{amu/D}$ to about $0.5\,\mathrm{amu/D}$. Figure 4.5 compares the performed sputter yield measurements with pure tungsten from chapter 4.2 with the resulting steady state mass removal rates of the WN targets. It is interesting to see, that at all three projectile energies the mass removal rate of the WN targets converges to the mass removal rate of the pure W targets. These measurements suggest a depletion of N from the WN targets during the D bombardment.

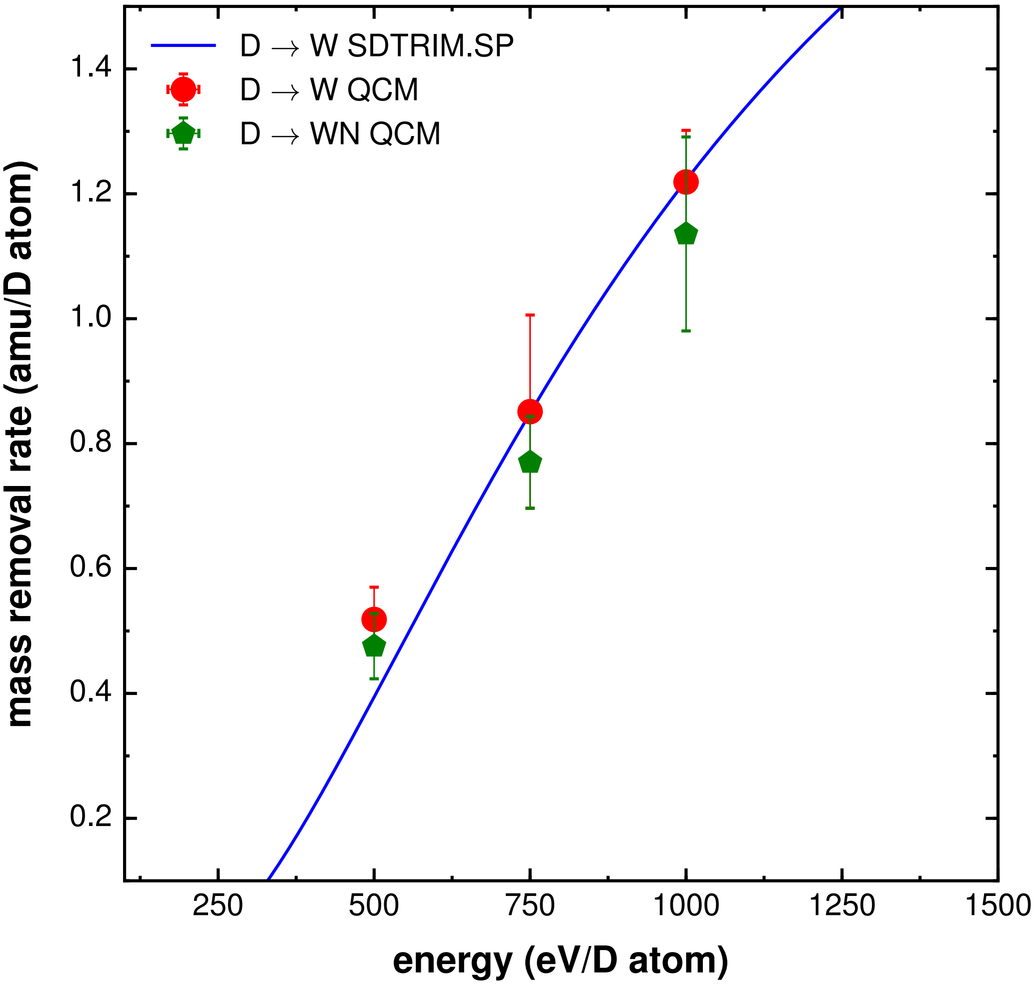

Figure 4.5 – Comparison of D → W sputter yield measurements at different energies to the equilibrium values of the D → WN mass removal rate measurements. The solid blue line represents an numerical simulation with SDTRIM.SP.

Dynamic sputtering calculations with SDTRIM.SP offer the possibility to simulate these measurements. Results are also plotted in figure 4.3 and figure 4.4, for better comparison with the performed measurements. The dynamic sputtering calculation at $500\,\mathrm{eV/D}$ confirms, that the WN mass removal rate converges to the pure W mass removal rate, but the required fluence is with about $0.4 \cdot 10^{23}\,\mathrm{D/m^2}$ higher. The calculated steady state mass removal rates are about 20% lower than the measured results, nevertheless they are at the border of the error areas and therefore plausible. It should be mentioned, that SDTRIM.SP delivers approximative results only, because effects like fluence dependent surface roughening, material diffusion and chemical sputtering are not included jet. All of these effects influence the sputtering behaviour.

The mass removal rate simulations at $1000\,\mathrm{eV/D}$ instead, shows a constant mass removal rate. No fluence dependence can be seen here at all. The resulting steady state mass removal rates are slightly higher than the measured results, but are still at the boundary of the error areas and therefore plausible.

SDTRIM.SP offers also the possibility to simulate the fluence dependence of the surface concentration of W and N. The result of this simulation can be seen in figure 4.6.

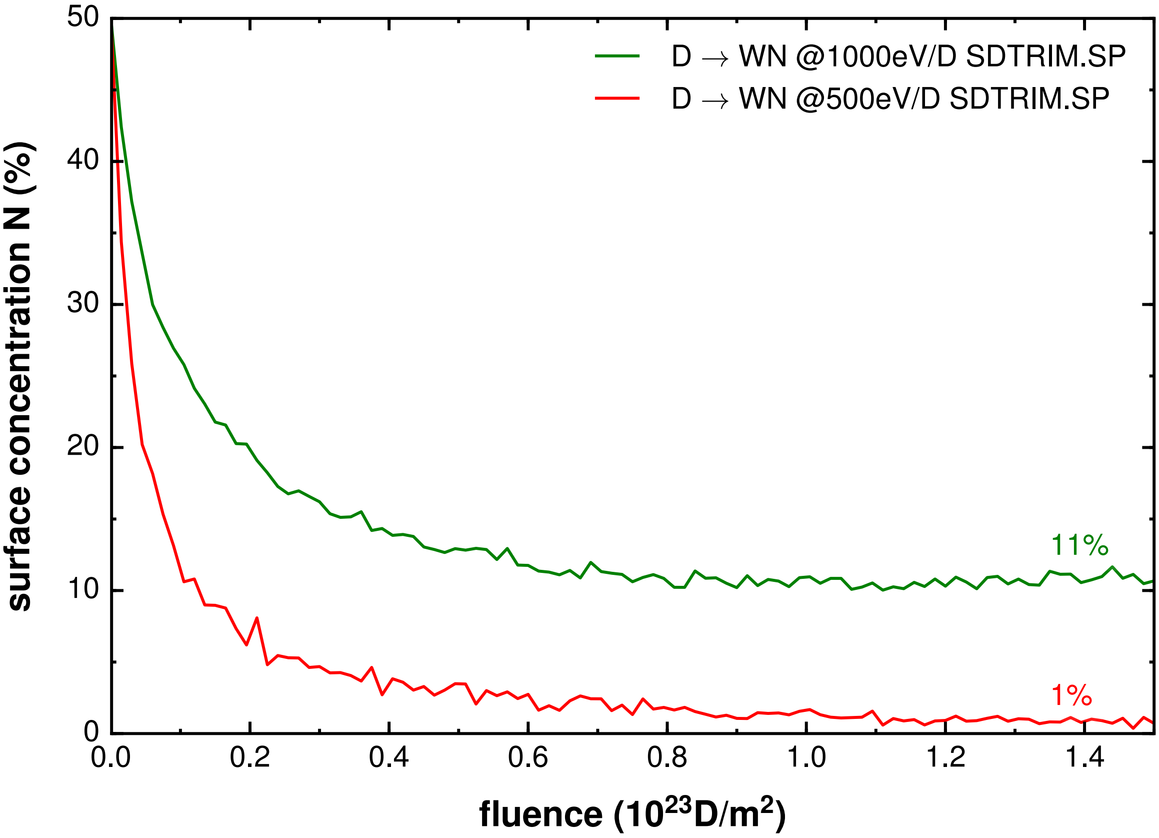

Figure 4.6 – SDTRIM.SP D on WN fluence dependent surface concentration calculation at $1000\,\mathrm{eV/D}$ and at $500\,\mathrm{eV/D}$, with an initial target composition of $50\ at.\%$ W and $50\ at.\%$ N. At both energies equilibrium is reached after a fluence of $0.6 \cdot 10^{23}\,\mathrm{D/m^2}$. The equilibrium surface concentration at $1000\,\mathrm{eV/D}$ is with 11% higher than at $500\,\mathrm{eV/D}$, with 1%.

The dynamic sputtering calculations with SDTRIM.SP (figure 4.6) show at $1000\,\mathrm{eV/D}$ and at $500\,\mathrm{eV/D}$ a significant decrease of the N surface concentration, which stands for a surface enrichment of W.

At $1000\,\mathrm{eV/D}$ an equilibrium of the surface composition is reached after about $0.6{\cdot}10^{23}\,\mathrm{D/m^2}$ at a surface composition of about $11\,\%$ N. The resulting equilibrium surface composition of N is caused on the one side by preferential sputtering of N and on the other side by implantation of recoiling N atoms into deeper layers of the bulk, which leads there to an increase of the N concentration [22].

Comparing this result to the performed measurement with $1000\,\mathrm{eV/D}$ in figure 4.3 shows, that it follows the same trend as the measured mass removal rate. The required fluence to reach steady state conditions is equal too and therefore it is likely, that the transient effect of the mass removal rate is caused by depletion of N from the surface.

Although the simulated surface concentration confirms the experimentally observed fluence dependece, SDTRIM.SP is not able to reproduce the transient effect of the mass removal rate at low fluences. This is caused by the fact, that these numerical simulations cannot include processes like chemical erosion and diffusion so far. Formation of ammonia (NH_3 or ND_3) and therefore chemical sputtering would explain the high mass removal rate at low fluences, where the surface composition of N is still high [22, 45]. Irradiation induced N diffusion was already reported in [17] and could also explain the enhanced N loss and therefore the higher mass removal rate at low fluences.

The calculation at $500\,\mathrm{eV/D}$ (figure 4.6) shows a nearly complete surface removal of N. After reaching a fluence of $0.6 \cdot 10^{23}\,\mathrm{D/m^2}$ the N surface concentration drops to about 1%. This amount of N at the surface is negligible small and therefore sputtering of a nearly pure W surface occurs. The performed measurement in figure 4.4 agrees with this explanation, but the required fluence is with $0.2 \cdot 10^{23}\,\mathrm{D/m^2}$ lower. This indicates, that the enhanced erosion of the surface at low fluences is also caused by additional N loss, may be due to chemical sputtering.

5 Transient Effects during Sputtering of FeW by D

In this chapter the erosion of pure Fe and FeW samples under impact of D ions are presented and discussed. The FeW samples have a compositon of $98.5\,\%$ Fe and $1.5\,\%$ W, which is a model system for EUROFER steel [27,28]. The first part describes the sample preparation. In the second part measurements with a pure Fe sample, at different ion energies and at different angle of incidence are presented. The third part presents high fluence FeW measurements at $1000\,\mathrm{eV/D}$ and $250\,\mathrm{eV/D}$ under normal incidence and discusses the results.

5.1 Preparation of Fe and FeW Samples

The Fe and FeW samples were prepared at the Max-Planck -Institute for Plasma Physics in Garching, Germany, by K. Sugiyama. A magnetron-sputter deposition device (Type Leybold UNIVEX 450B) was used, to cover one of the gold electrodes of the virgin quartz crystals with the desired layer composition. The used sample preparation holder was the same as described in the last chapter (figure 4.1). The magnetron-sputter deposition device uses Argon as working gas and multiple sputtering targets with variable input power for each, to perform the required layer composition of $98.5\,\mathrm{at.\%}$ Fe and $1.5\,\mathrm{at.\%}$ W and a layer thickness of about $400\,\mathrm{nm}$.

The layer composition was checked by using Rutherford backscattering spectroscopy (RBS) with ^{4}He ions. The Results confirmed the layer composition, but showed also an concentration of about $1-2\,\mathrm{at.\%}$ O. Ar impurities were below detection limit [27].

5.2 Sputtering of Fe by D

A pre-step for investigating the erosion of FeW alloys is to know the sputtering behaviour of pure W and pure Fe. Sputtering measurements of pure W by D have already been performed in the last chapter and the results can be found there (chapter 4.2).

Table 5.1 shows the measured D on Fe sputter yields at different energies and figure 5.1

compares these measurements with data from literature. Next to these normal incidence measurements, angular dependent sputter yield measurements were performed and presented in section 5.2.1.

Table 5.1 – D → Fe sputter yields measurement results at different ion energies.

ion energy $[\mathrm{eV/D}]$	mass removal rate $[\mathrm{amu/D}]$	sputter yield $[\cdot 10^{-2}\,\mathrm{Fe/D}]$
250	1.39 ± 0.13	2.5 ± 0.2
500	2.46 ± 0.21	4.4 ± 0.4
750	2.97 ± 0.28	5.3 ± 0.5
1000	3.14 ± 0.35	5.6 ± 0.6

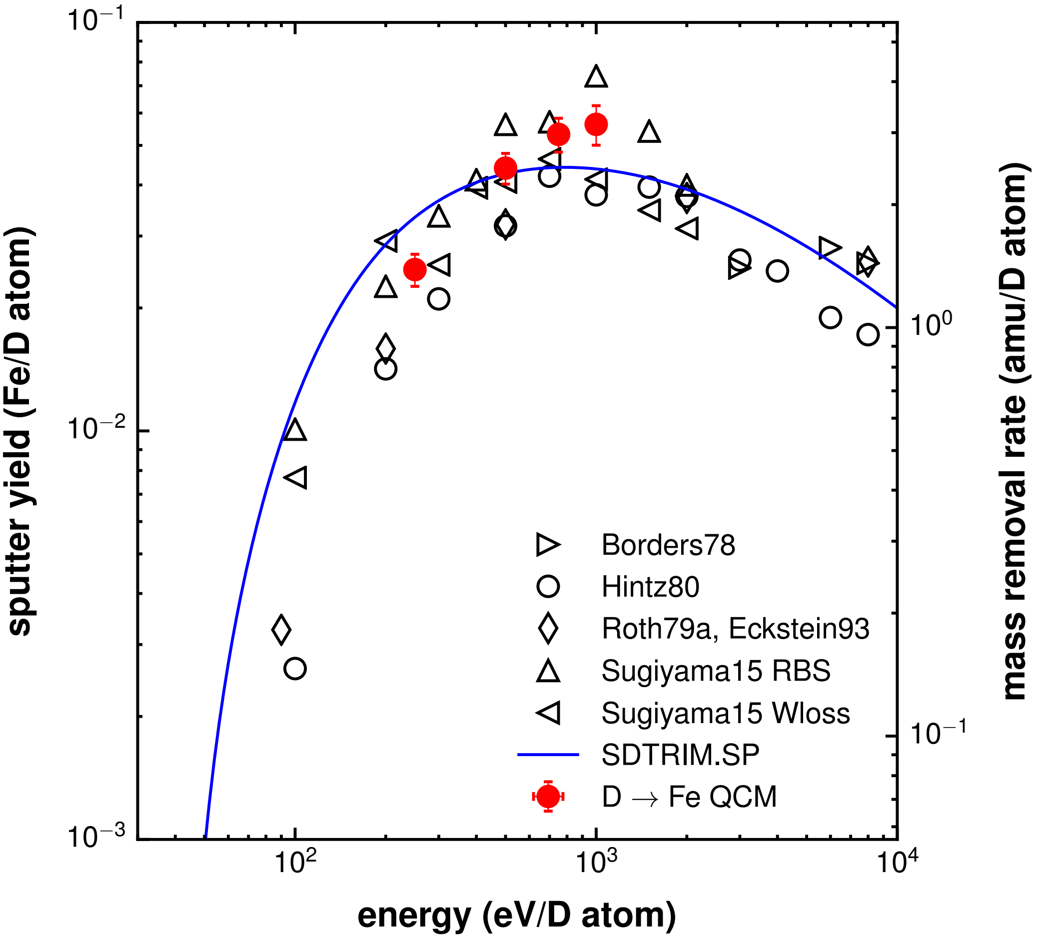

Figure 5.1 – D → Fe sputter yield measurements at different energies and normal incidence compared to other experiments from literature [30, 44]. The solid line represents a static SDTRIM.SP simulation.

Comparing the results with data from literature and other experiments (figure 5.1) shows, that the measured D → Fe mass removal rates are consistent with them and therefore rather plausible. The static sputtering calculations with SDTRIM.SP describes the energy dependence of the sputter yield also quite good and show the same trend as other experiments.

5.2.1 Angle of Incidence Dependent Sputtering of Fe by D

In this chapter sputtering measurements, as a function of the incident ion angle are presented and discussed. These measurements were done on the one hand to test the experimental setup and on the other hand to know the angular dependent behaviour of sputtering a pure Fe film by D. This is an essential pre-step for angular dependent measurements of FeW targets.

The measurements were performed in steps of $15\,°$ (with respect to the surface normal), starting from $0\,°$. The maximum possible impact angle is limited to $70\,°$, by design of the QCM holder. Results can be seen in table 5.2 and in figure 5.2.

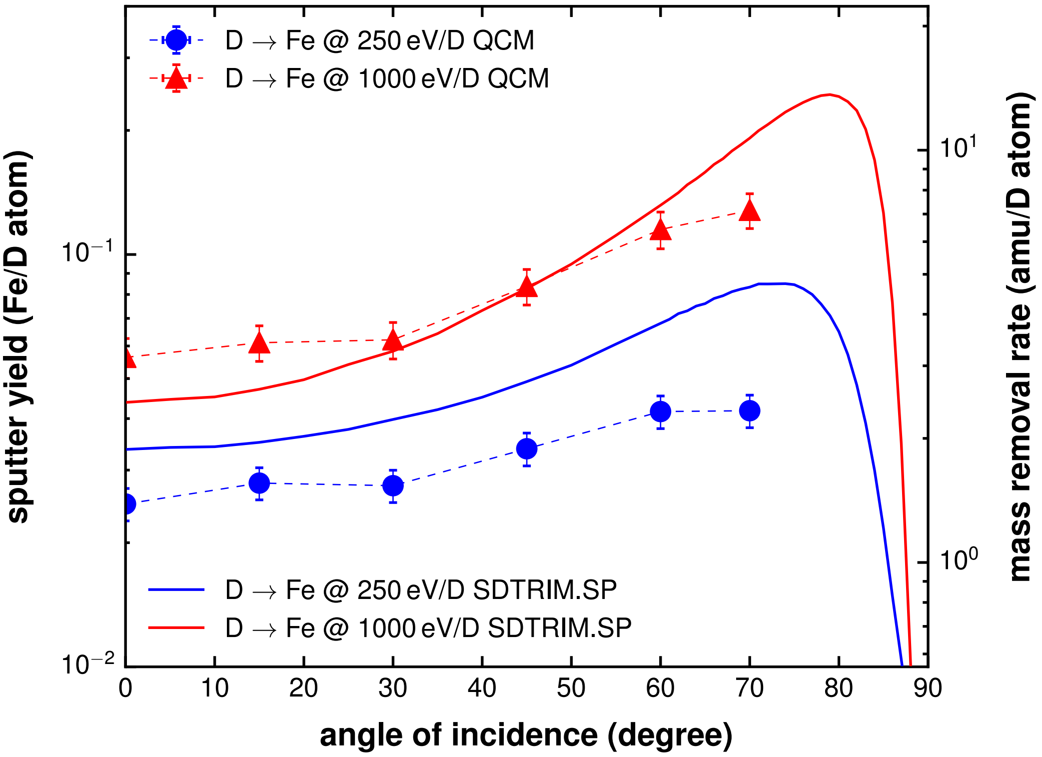

Figure 5.2 – D → Fe sputter yield measurements at different angle of incidence (with respect to the surface normal) at projectile energies of $250\,\mathrm{eV/D}$ and $1000\,\mathrm{eV/D}$. The solid lines represent SDTRIM.SP simulations.

Table 5.2 – D → Fe sputter yields measurement results at different angle of incidence (with respect to the surface normal) and two different D ion energies. These measurements were performed after a D fluence of about $1.5 \cdot 10^{23}\,\mathrm{D/m^2}$.

angle of incidence [degree]	sputter yield @ $250\,\mathrm{eV/D}$ $[\cdot 10^{-2}\,\mathrm{Fe/D}]$	sputter yield @ $1000\,\mathrm{eV/D}$ $[\cdot 10^{-2}\,\mathrm{Fe/D}]$
0	2.5 ± 0.2	5.6 ± 0.6
15	2.8 ± 0.3	6.1 ± 0.6
30	2.8 ± 0.3	6.2 ± 0.6
45	3.4 ± 0.3	8.4 ± 0.8
60	4.1 ± 0.4	11.5 ± 1.2
70	4.2 ± 0.4	12.8 ± 1.2

No data for comparison could be found in literature for angular dependent sputter yield measurements of Fe by D, therefore only comparison to dynamic sputtering calculations with SDTRIM.SP were possible (figure 5.2).

At $1000\,\mathrm{eV/D}$ as well as at $250\,\mathrm{eV/D}$ the measurements show an increase in the sputter yield at higher angles of impact, which was expected. Steeper ion impact angles usually lead to a higher sputter yield, because the induced collision cascade stays more closer to the target surface and therefore the sputter probability is much higher [30]. This trend agrees with the dynamic sputtering calculations with SDTRIM.SP, but these simulation predict even higher sputter yields at higher angles of impact.

SDTRIM.SP cannot include effects like fluence dependent surface roughening jet, which influences the sputtering behaviour too. Surface roughness of the target smooths the angular dependence of the sputter yield. A focused and parallel ion beam hitting a rough surface can be estimated as an ion beam with a certain angular distribution, hitting a perfect flat surface. This means a sputter yield measurement at a certain angle of incidence on a target with a certain surface roughness is equal to a superposition of sputter yield measurements at various angles of incidence, which explains this smoothed angular dependence. More surface roughness dependent sputter yield measurements and investigations are planned in future.

5.3 Sputtering of FeW by D

Comparing table 4.1 with table 5.1 shows, that the sputter yield of pure Fe by D at an ion energy of $1000\,\mathrm{eV/D}$ is about 8.5 times higher than sputtering pure W. At $500\,\mathrm{eV/D}$ this factor increases to 16 and at $250\,\mathrm{eV/D}$ sputtering of W by D could not be measured at all. Therefore the effect of preferential sputtering of Fe and a resulting surface enrichment of W is expected to be visible at low energies.

At first high fluence measurements were performed under normal incidence and at an ion energie of $1000\,\mathrm{eV/D}$. Results can be found in figure 5.3. After that the same measurement was performed at an ion energy of $250\,\mathrm{eV/D}$ and the results can be found in figure 5.4.

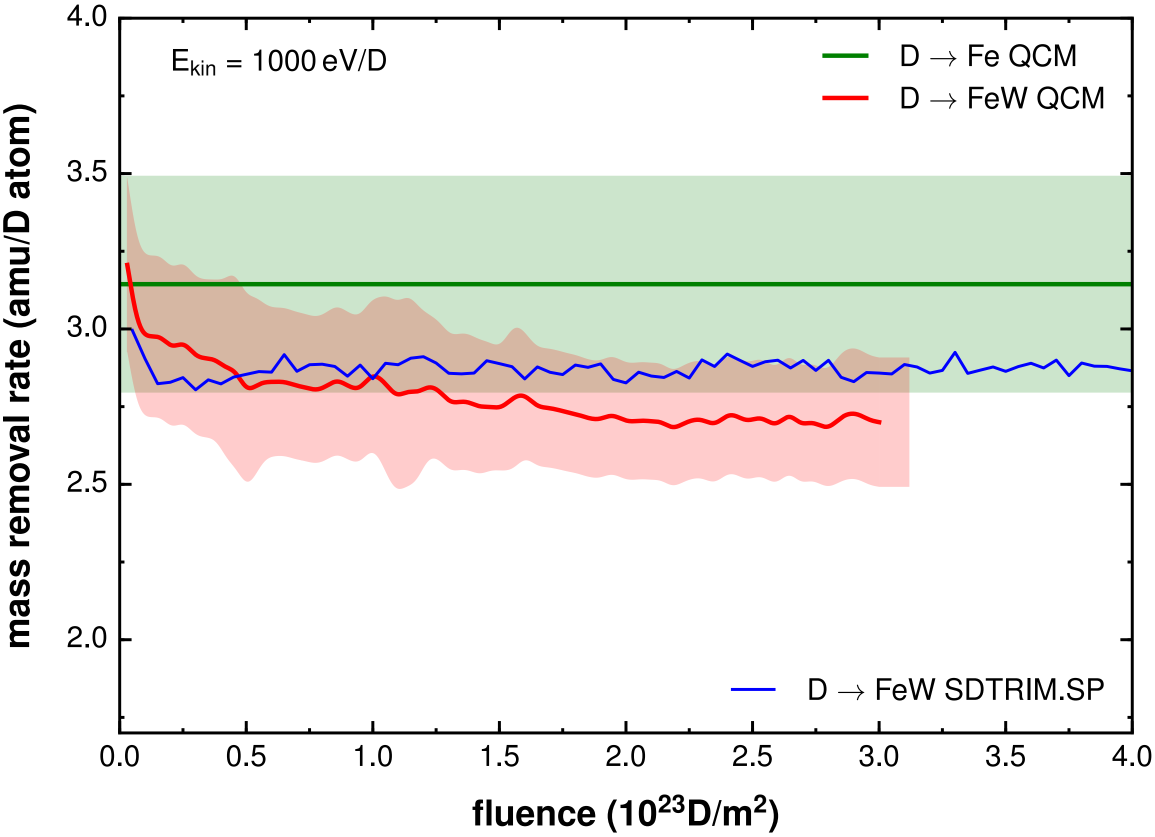

Figure 5.3 – D → FeW fluence dependent mass removal rate measurement at an kinetic ion energy of $1000\,\mathrm{eV/D}$ and an ion flux of $3 \cdot 10^{18}\,\mathrm{D/m^2/s}$. The red graph is a weighted average of 4 measurements. The green graph represents a D → Fe measurement, which is assumed to be constant. At low fluences the mass removal rate of FeW is close to the mass removal rate of pure Fe, but decreases with higher fluences. After about $2 \cdot 10^{23}\,\mathrm{D/m^2}$ the mass removal rate reaches a nearly constant value of about $2.7\,\mathrm{amu/D}$. The light-green and light-red areas represent the possible error and the blue line shows a dynamic sputtering calculation with SDTRIM.SP.

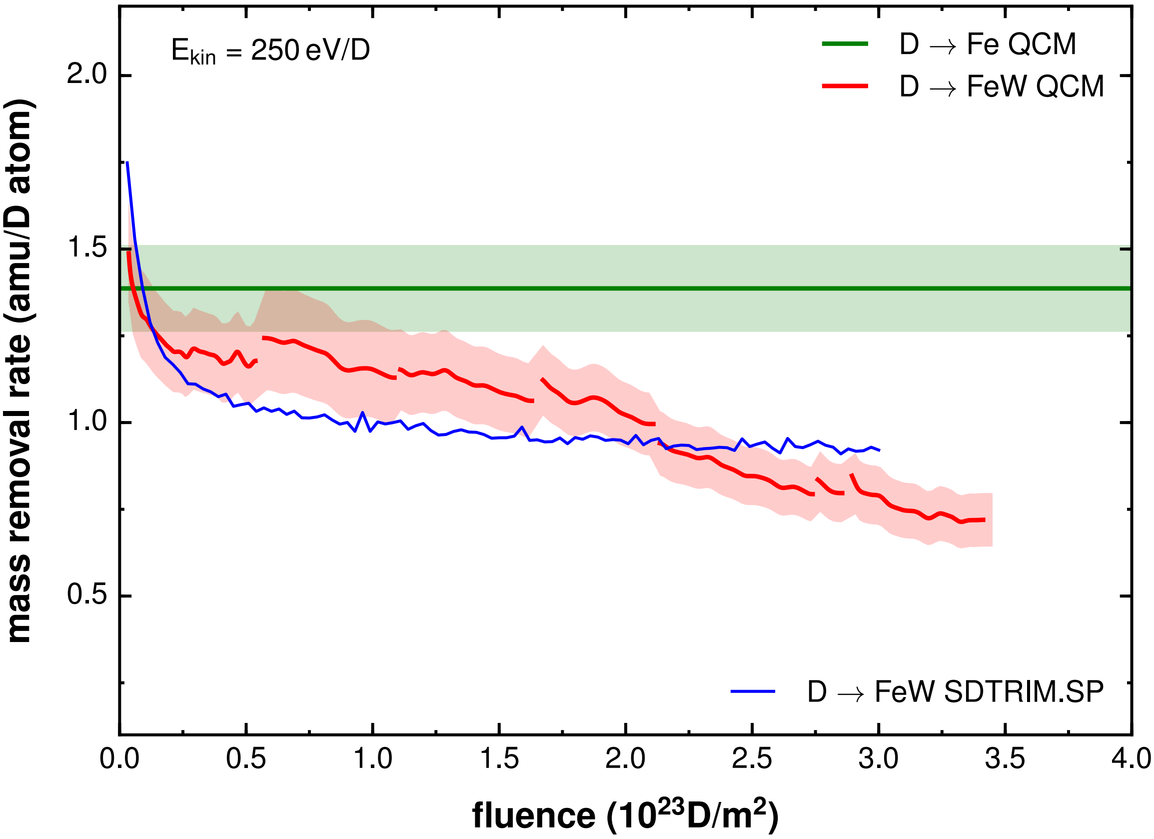

Figure 5.4 – D → FeW fluence dependent mass removal rate measurement at an kinetic ion energy of $250\,\mathrm{eV/D}$ and an ion flux of $8 \cdot 10^{17}\,\mathrm{D/m^2/s}$. The ion current was checked after every fluence step, which causes short interrupts between the measurements. The green graph represents a D → Fe measurement, which is assumed to be constant. The mass removal rate of the FeW target drops quickly at low fluences. After about $0.25 \cdot 10^{23}\,\mathrm{D/m^2}$ the slope of the mass removal rate reaches a nearly constant value. The mass removal rate continuously drops with increasing fluence and even after a fluence of about $3.5 \cdot 10^{23}\,\mathrm{D/m^2}$ no steady state conditions can be seen. The light-green and the light-red areas represent the possible error and the blue line a dynamic sputtering calculation with SDTRIM.SP.

Both FeW measurements show a transient effect of the mass removal rate with increasing fluence. At $1000\,\mathrm{eV/D}$ (figure 5.3) and at low fluences the the mass removal rate of the FeW targets are close to the value of pure Fe, which is caused by the fact that the sample composition is $98.5\,\mathrm{at.\%}$ Fe. With increasing fluence the mass removal rate drops and reaches a nearly constant value of $2.7\,\mathrm{amu/D}$, after a flunce of about $2 \cdot 10^{23}\,\mathrm{D/m^2}$. The sputter threshold energy for Fe by D is about $40\,\mathrm{eV}$ and for W by D about $230\,\mathrm{eV}$. Therefore at $1000\,\mathrm{eV/D}$ the energy is high enough to sputter both elements and the surface enrichment of W stops as soon as the partial sputter yields reach equilibrium [30].
A dynamic sputtering calculation with SDTRIM.SP at $1000\,\mathrm{eV/D}$ reaches this steady state mass removal rate already at about $1 \cdot 10^{23}\,\mathrm{D/m^2}$ and predicts a $5\,\%$ higher mass removal

rate than measured. At low fluences the simulation does not reproduce the transient effect of the real measurement, nevertheless the steady state mass removal rate is in the range of the error-areas and therefore plausible.

The measurement at $250\,\mathrm{eV/D}$ (figure 5.4) is of high interest, because the particle energies in the recessed areas of a future fusion reactor is expected to be below $200\,\mathrm{eV/D}$ [28]. The D ion energy of $250\,\mathrm{eV/D}$ is only $15\,\%$ higher than the sputter threshold energy for sputtering pure W by D and therefore the probability to sputter W should be low [30]. Lower energies are not possible by design of the ion source.
The starting value of the mass removal rate of the FeW sample is about the mass removal rate of the pure Fe sample. It drops quickly from about $2\,\mathrm{amu/D}$ to about $1.2\,\mathrm{amu/D}$, after a fluence of $0.25 \cdot 10^{23}\,\mathrm{D/m^2}$ only. After this fluence step the slop of the mass removal rate reduces and reaches a nearly constant value. Even after about $3.5 \cdot 10^{23}\,\mathrm{D/m^2}$ no equilibrium of the mass removal rate can be seen, but the slope of the removal rate gets lower. It would be very interesting to perform measurements at even higher fluences, but due to the limited thickness of the sample film on top of the quartz crystal this is not possible with the QCM technique.
The dynamic sputtering calculation with SDTRIM.SP at $250\,\mathrm{eV/D}$ agrees at low fluences with the measurement quite well, but the predicted steady state mass removal rate after a fluence of about $1.5 \cdot 10^{23}\,\mathrm{D/m^2}$ cannot be confirmed by the measurement. This could be due to the fact, that at lower ion energies the BCA in SDTRIM.SP reaches a limit and other interaction effects need to be taken into account to get more accurate sputter yield calculations.

6 Summary and Outlook

The possibility to use a sputter gun as an ion source in combination with the existing QCM technology allows a small and comparatively cheap setup for sputter yield measurements at high fluences. The comparison measurements with the existing ECR ion source SOPHIE have shown, that the new setup delivers useful results in a fraction of time. A maximum flux of $2.7 \cdot 10^{18}\,\mathrm{D/m^2/s}$ could be achieved, which allows to reach a fluence of $1 \cdot 10^{23}\,\mathrm{D/m^2}$ in 11 hours only. A residual gas pressure of about $1.7 \cdot 10^{-5}\,\mathrm{mbar}$ in the area of the QCM holder is quite high and leads to a continuous coverage of the sample with the working gas D. However, these conditions are comparable to the interior of a working TOKAMAK and can be seen as an advantage.

A redesign of the QCM holder allows now more accurate ion current measurements, due to including a secondary electron suppressor and therefore more accurate sputter yield measurements. Furthermore this redesign allows varying the angle of incidence up to $70\,^\circ$ (with respect to the surface normal) and makes angular dependent sputter yield measurements possible.

Erosion of WN Surfaces:

The evolution of the mass removal rate of WN films with a 1:1 concentration ratio have been measured and compared to the mass removal rates of a pure W film. The measured results have been summarized in figure 6.1. Both measurements showed transient effects of the mass removal rate. At a kinetic projectile energy of $1000\,\mathrm{eV/D}$ the mass removal rate approaches that of pure W, after a fluence of about $0.6 \cdot 10^{23}\,\mathrm{D/m^2}$.

At $500\,\mathrm{eV/D}$ the same effect can be observed, but the required fluence is with about $0.2 \cdot 10^{23}\,\mathrm{D/m^2}$ lower. Comparing these measurements with dynamic sputtering calculations with SDTRIM.SP showed, that the surface concentration of N follows the same trend as the mass removal rate. This indicates a depletion of N from the sample surface. However SDTRIM.SP was not able to reproduce the transient effects of the mass removal rate. These numerical simulations cannot include processes like chemical erosion and diffusion so far. D induced diffusion and chemical sputtering in form of formation of ammonia (NH_3 or ND_3) at the surface would explain the high mass removal rate at low fluences, where the surface composition of N is still high [22, 45].

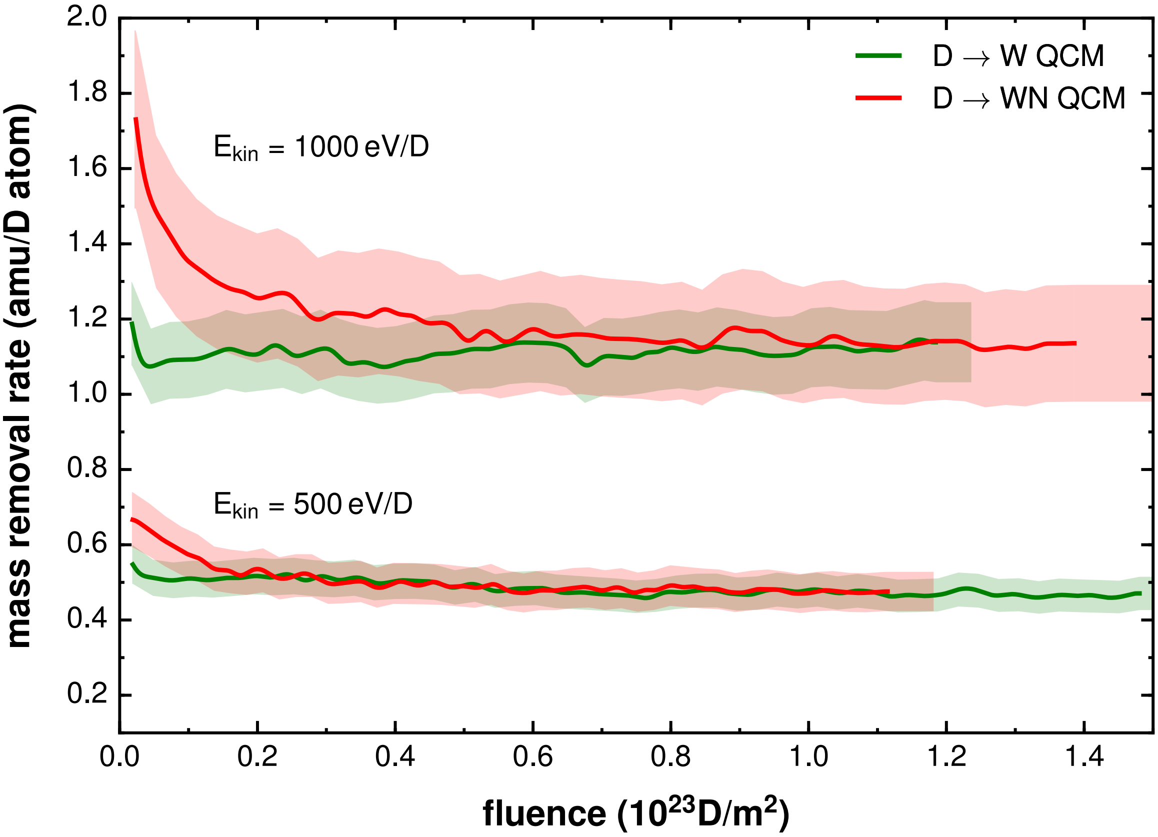

Figure 6.1 – D → W and D → WN mass removal rate measurements at kinetic projectile energies of $1000\,\mathrm{eV/D}$ and $500\,\mathrm{eV/D}$. At $1000\,\mathrm{eV/D}$ the mass removal rate of the WN sample converges to the mass removal rate of pure W, after a fluence of about $0.6 \cdot 10^{24}\,\mathrm{D/m^2}$. At $500\,\mathrm{eV/D}$ the same effect can be seen, but the required fluence is with about $0.2 \cdot 10^{24}\,\mathrm{D/m^2}$ lower. The light-red and light green areas represent the possible error.

Erosion of FeW Surfaces:

The interaction of D projectiles with FeW model films, with $1.5\,\mathrm{at.\,\%}$ W have been measured and compared to the results of pure Fe films. The measurements were performed at kinetic projectile energies of $1000\,\mathrm{eV/D}$ and $250\,\mathrm{eV/D}$. Results can be found in figure 6.2. For low D fluences the mass removal rate of FeW is close to the value of pure Fe. With increasing D fluence a reduction of the mass removal rate is observed. At $1000\,\mathrm{eV/D}$ after reaching a fluence of about $2 \cdot 10^{23}\,\mathrm{D/m^2}$ a nearly constant mass removal rate of about $2.7\,\mathrm{amu/D}$ can be seen. Due to the higher sputter yield of Fe by D, compared to W by D, a preferential sputtering of Fe occurs, which leads to a surface enrichment of W. At $1000\,\mathrm{eV/D}$ the projectile energy is high enough to sputter Fe as well as W and so the surface enrichment of W stops after reaching a certain surface concentration [30].
At $250\,\mathrm{eV/D}$ the projectile energy is close to the threshold energy of sputtering W by D,

and therefore the probability of sputtering W by D is extremely low. Therefore the effect of preferential sputtering of Fe is very strong here and the surface enrichment of W leads to a continuous reduction of the mass removal rate. Even after a fluence of about $3.5 \cdot 10^{23}\,\mathrm{D/m^2}$ no equilibrium of the mass removal rate can be seen. This measurement is of high interest, because the expected particle energies in recessed areas of a future fusion reactor is expected to be below $200\,\mathrm{eV/D}$ [28]. Therefore FeW alloys should be able to be used as a wall material in a fusion reactor and can reduce the cost of the reactor vessel.

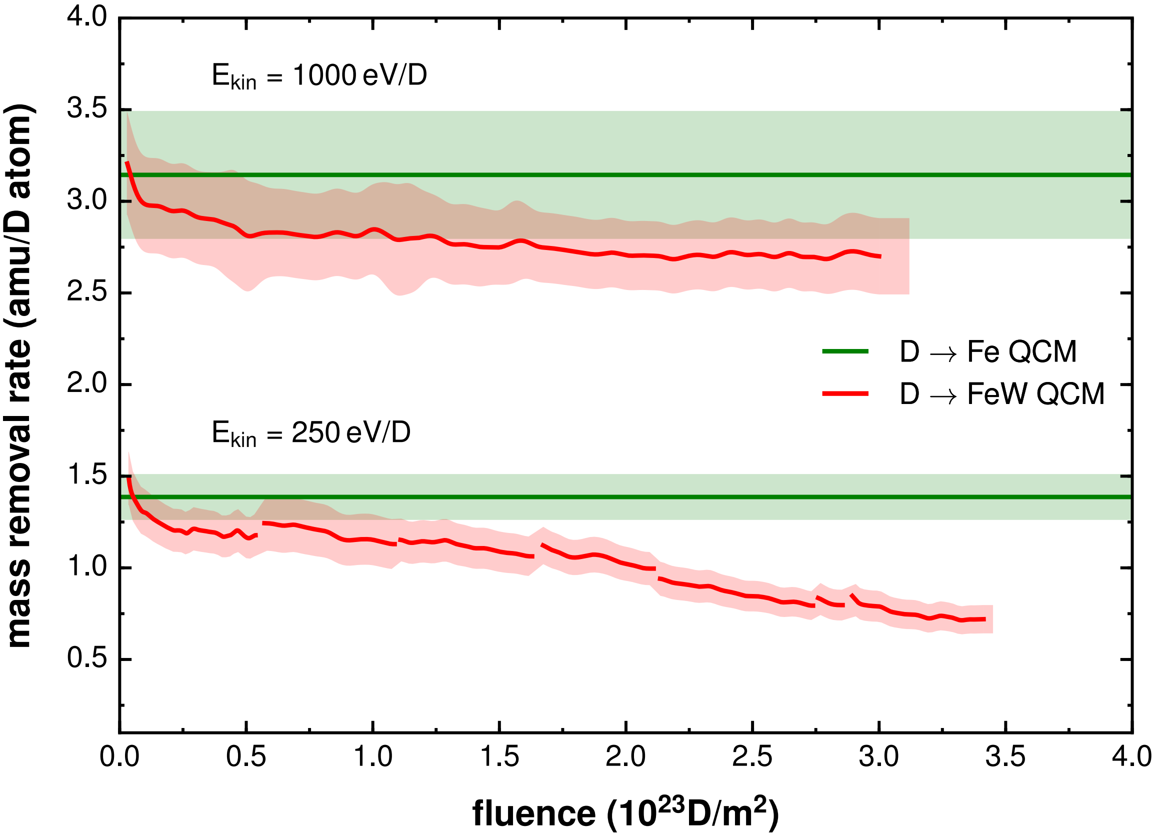

Figure 6.2 – D → Fe and D → FeW mass removal rate measurements at projectile energies of $1000\,\mathrm{eV/D}$ and $250\,\mathrm{eV/D}$. The green graph represents D → Fe measurements, which are assumed to be constant over fluence. Both FeW measurements show a reduction of the mass removal rate with increasing fluence, starting at the value of pure Fe. At $1000\,\mathrm{eV/D}$ a steady state mass removal rate of $2.7\,\mathrm{amu/D}$ is observed, while at $250\,\mathrm{eV/D}$ no steady state conditions can be seen. The light-red and light green areas represent the possible error.

As a pre step for investigating the sputter behaviour of FeW samples as a function of the ion incident angle, measurements were performed with a pure Fe sample ($0\,° - 70\,°$, with respect to the surface normal). At $250\,\mathrm{eV/D}$ the sputter yield increases from $2.5 \pm 0.2\,\mathrm{Fe/D}$ (@ $0\,°$) to $4.2 \pm 0.4\,\mathrm{Fe/D}$ (@ $70\,°$) and at $1000\,\mathrm{eV/D}$ a similar increase of the sputter yield can be seen. The mass removal rate starts from about $5.6 \pm 0.6\,\mathrm{Fe/D}$ (@ $0\,°$) and raises to about $12.8 \pm 1.2\,\mathrm{Fe/D}$ (@ $70\,^\circ$). Larger ion impact angles usually lead to a higher sputter yield, because the induced collision cascade stays more closer to the target surface and therefore the sputter probability is much higher [30]. Effects like fluence dependent surface roughening lead to a smoothing of the angular dependence of the sputter yield and is topic of current research. More surface roughness dependent sputter yield measurements and investigations are therefore planned in the near future.

Acronyms

ASCII American Standard Code for Information Interchange

ASDEX Upgrade Axially Symmetric Divertor Experiment

BCA Binary Collision Approximation

CAD Computer Aided Design

CF Conflat

ECR Electron Cyclotron Resonance

Excel spreadsheet software

FC Faraday Cup

ITER International Thermonuclear Experimental Reactor

JET Joint European Torus

LabVIEW Laboratory Virtual Instrumentation Engineering Workbench (Software)

PC Personal Computer

PFC plasma facing components

PYTHON script based high level programming language `www.python.org`

QCM Quartz Crystal Microbalance

RBS Rutherford Backscattering Spectroscopy

SDTRIM.SP Static and Dynamic TRIM Sequential and Parallel (Software)

SOPHIE Source for Producing Highly Charged Ions using ECR

TOF-ERDA Time of Flight Elastic Recoil Detection Analysis

TRIDYN Dynamic Transport of Ions in Matter

TRIM Transport of Ions in Matter

TOKAMAK Toroidal Chamber with Magnetic Coils (russian: ТОроидальная КАмера с МАгнитными Катушками)

UHV Ultra High Vacuum

Bibliography

[1] Cook I., Marbach G., Pace L.D., Girard C., Rocco P. and Taylor N., 'Results, conclusions, and implications of the SEAFP-2 programme', *Fusion Engineering and Design*, **51–52**, 409 (2000)

[2] 'ITER organization', URL `www.iter.org`

[3] 'European Consortium for the Development of Fusion Energy', URL `www.euro-fusion.org`

[4] Lawson J.D., 'Some Criteria for a Power Producing Thermonuclear Reactor', *Proceedings of the Physical Society B*, **70**, 6 (1957)

[5] Dobeš K., 'Erosion of Fusion Relevant Surfaces under Ion Impact', Ph.D. thesis, Vienna University of Technology (2014)

[6] Boozer A.H., 'Physics of magnetically confined plasmas', *Rev. Mod. Phys.*, **76**, 1071 (2005)

[7] Janeschitz G., ITER JCT and HTs, 'Plasma-Wall Interaction Issues in ITER', *Journal of Nuclear Materials*, **290** - **293**, 1 (2001)

[8] Janeschitz G., Borrass K., Federici G., Igitkhanov Y., Kukushkin A., Pacher H., Pacher G. and Sugihara M., 'The ITER divertor concept', *Journal of Nuclear Materials*, **220–222**, 73 (1995)

[9] Dux R., Bobkov V., Herrmann A., Janzer A., Neu R., Mayer M., Müller H.W., Pugno R., Pütterich T., Rhode V., Sips A.C.C. and the ASDEX Upgrade Team, 'Plasma-Wall Interaction and Plasma Behaviour in the Boronised All Tungsten Wall', *Journal of Nuclear Materials*, **390** - **391**, 858 (2009)

[10] Kallenbach A., Dux R., Fuchs J.C., Fischer R., Geiger B., Giannone L., Herrmann A., Lunt T., Mertens V., McDermott R., Neu R., Pütterich T., Rathgeber S., Rohde V., Schmid K., Schweinzer J., Treutterer W. and the ASDEX Upgrade Team, 'Divertor Power Load Feedback with Nitrogen Seeding in ASDEX Upgrade', *Plasma Physics and Controlled Fusion*, **52**, 055002 (2010)

[11] Kallenbach A., Balden M., Dux R., Eich T., Girard C., Huber A., Maddison G.P., Mayer M., McCormick K., Neu R., Petrie T.W., Pütterich T., Rapp J., Reinke M.L., Schmid K., Schweinzer J., Wolfe S., the ASDEX-Upgrade Team, DIII-D Team, Alcator Team and JET-EFDA contributors, 'Plasma Surface Interactions in Impurity Seeded Plasmas', *Journal of Nuclear Materials*, **415**, S19 (2011)

[12] Neu R., Arnoux G., Beurskens M., Bobkov V., Brezinsek S., Bucalossi J., Calabro G., Challis C., Coenen J.W., de la Luna E., de Vries P.C., Dux R., Frassinetti L., Giroud C., Groth M., Hobrik J., Joffrin E., Lang P., Lehnen M., Lerche E., Loarer T., Lomas P., Maddison G., Maggi C., Matthews G., Marsen S., Mayoral M.L., Meigs A., Mertens P., Nunes I., Philipps V., Pütterich T., Rimini F., Sertoli M., Sieglin B., Sips A.C.C., van Eester D., van Rooij G. and JET-EFDA contributors, 'First Operation with the JET International Thermonuclear Experimental Reactor-Like Wall', *Physics of Plasmas*, **20**, 056111 (2013)

[13] Oberkofler M., Douai D., Brezinsek S., Coenen J.W., Dittmar T., Drenik A., Romanelli S.G., Joffrin E., McCormick K., Brix M., Calabro G., Clever M., Giroud C., Kruezi U., Lawson K., Linsmeier C., Rojo A.M., Meigs A., Marsen S., Neu R., Reinelt M., Sieglin B., Sips G., Stamp M., Tabarés F.L. and the EFDA-JET contributors, 'First Nitrogen-Seeding Experiments in JET with the ITER-like Wall', *Journal of Nuclear Materials*, **438**, S258 (2013)

[14] Roth J., Tsitrone E., Loarte A., Loarer T., Consell G., Neu R., Philipps V., Brezinsek S., Lehnen M., Coad P., Grisola C., Schmid K., Krieger K., Kallenbach A., Lipschultz B., Doerner R., Causey R., Alimov V., Shu W., Ogorodnikova O., Kirschner A., Federici G. and Kukushkin A., 'Recent Analysis of Key Plasma Wall Interactions Issues for ITER', *Journal of Nuclear Materials*, **390 - 391**, 1 (2009)

[15] Dobes K., Naderer P., Lachaud N., Eisenmenger-Sittner C. and Aumayr F., 'Sputtering of Tungsten by N^+ and N_2^+ Ions: Investigations of Molecular Effects', *Physica Scripta*, **T145**, 014017 (2011)

[16] Schmid K., Manhard A., Linsmeier C., Wiltner A., Schwarz-Selinger T., Jacob W. and Mändl S., 'Interaction of Nitrogen Plasmas with Tungsten', *Nuclear Fusion*, **50**, 025006 (2010)

[17] Meisl G., Schmid K., Encke O., Höschen T., Gao L. and Linsmeier C., 'Implantation and erosion of nitrogen in tungsten', *New Journal of Physics*, **16**, 093018 (2014)

[18] Schwarz-Seilinger G.M.T., 'Joint WP JET2 / WP PFC Annual Meeting 2014', in *Report on PFC SP2, PWI Processes I: erosion, deposition and mixing: SDTRIM.SP results of D on WN*, 40, EUROfusion (2014)

[19] Hayderer G., Schmid M., Varga P., Winter H.P. and Aumayr F., 'A Highly Sensitive Quartz-Crystal Microbalance for Sputtering Investigations in Slow Ion-Surface Collisions', *Review of Scientific Instruments*, **70**, 3696 (1999)

[20] Sauerbrey G., 'Verwendung von Schwingquarzen zur Wägung dünner Schichten und zur Mikrowägung', *Zeitschrift für Physik*, **155**, 206 (1959)

[21] Galutschek E., Trassl R., Salzborn E., Aumayr F. and Winter H.P., 'Compact 14.5 GHz All-Permanent Magnet ECRIS for Experiments with Slow Multicharged Ions', *Journal of Physics Conference Series*, **58**, 395 (2007)

[22] Berger B.M., Stadlmayr R., Meisl G., Cekada M., Eisenmenger-Sittner C., Schwarz-Selinger T. and Aumayr F., 'Transient effects during erosion of WN by deuterium ions studied with the quartz crystal microbalance technique', *Nuclear Instruments and Methods in Physics Research Section B* (2016), in preparation

[23] Perkin Elmer, *PHI Model 04-161 Sputter Ion Gun and PHI Model 20-045 Sputter Ion Gun Control Technical Manual* (1980)

[24] Maisonnier D., Cook I., Pierre S., Lorenzo B., Edgar B., Karin B., Luigi D.P., Robin F., Luciano G., Stephan H., Claudio N., Prachai N., Aldo P., Neill T. and David W., 'The European power plant conceptual study', *Fusion Engineering and Design*, **75–79**, 1173 (2005)

[25] Bolt H., Barabash V., Federici G., Linke J., Loarte A., Roth J. and Sato K., 'Plasma Facing and High Heat Flux Materials - Needs for ITER and Beyond', *Journal of Nuclear Materials*, **307 - 311**, 43 (2002)

[26] van der Schaaf B., Tavassoli F., Fazio C., Rigal E., Diegele E., Lindau R. and LeMarois G., 'The development of EUROFER reduced activation steel', *Fusion Engineering and Design*, **69**, 197 (2003)

[27] Sugiyama K., Roth J., Alimov V., Schmid K., Balden M., Elgeti S., Koch F., Höschen T., Baldwin M., Doerner R., Maier H. and Jacob W., 'Erosion study of Fe-W binary mixed layer prepared as model system for RAFM steel', *Journal of Nucler Materials*, **463** (2015)

[28] Roth J., Sugiyama K., Alimov V., Höschen T., Baldwin M. and Doerner R., 'EUROFER as wall material: Reduced sputtering yields due to W surface enrichment', *Journal of Nuclear Materials*, **454**, 1 (2014)

[29] Sigmund P., *Sputtering by Particle Bombardment I*, chapter Sputtering by Ion Bombardment Theoretical Concepts, 9, Topics of Applied Physics, Springer Berlin, Heidelberg (1981)

[30] Behrisch R. and Eckstein W., eds., *Sputtering by Particle Bombardment*, volume 110 of *Topics in Applied Physics*, Springer Berlin Heidelberg (2007)

[31] Roth J., *Nuclear Fusion Research*, volume 78 of *Springer Series in Chemical Physics*, chapter Review and Status of Physical Sputtering and Chemical Erosion of Plasma Facing Materials, 203 – 225, Springer Berlin, Heidelberg (2005)

[32] Aumayr F. and Winter H., 'Potential sputtering', *Philosophical Transactions of the Royal Society of London A: Mathematical, Physical and Engineering Sciences*, **362**, 77 (2004)

[33] Schmid M., Benes E., Burger W. and Kravchenko V., 'Motional capacitance of layered piezoelectric thickness-mode resonators', *Ultrasonics, Ferroelectrics, and Frequency Control, IEEE Transactions on*, **38**, 199 (1991)

[34] 'KVG Quartz Crystal Technology GmbH 2015', URL `www.kvg-gmbh.de`

[35] Mutzke A., Schneider R., Eckstein W. and Dohmen R., 'SDTrimSP Version 5.00', *Report IPP*, **12/8** (2011)

[36] Biersack J. and Haggmark L., 'A Monte Carlo computer program for the transport of energetic ions in amorphous targets', *Nuclear Instruments and Methods*, **174**, 257 (1980)

[37] Biersack J.P. and Eckstein W., 'Sputtering studies with the Monte Carlo Program TRIM.SP', *Applied Physics A*, **34**, 73 (1984)

[38] Eckstein W., *Computer Simulation of Ion - Solid Interactions*, volume 10 of *Springer Series in Materials Sicence*, Springer Berlin, Heidelberg (1991)

[39] Möller W. and Eckstein W., 'Tridyn — A TRIM simulation code including dynamic composition changes', *Nuclear Instruments and Methods in Physics Research Section B: Beam Interactions with Materials and Atoms*, **2** (1984)

[40] Möller W., Eckstein W. and Biersack J., 'Tridyn-binary collision simulation of atomic collisions and dynamic composition changes in solids', *Computer Physics Communications*, **51**, 355 (1988)

[41] Colutron Research Corporation, *Velocity Filter Model 600, 600-H, 600-B, 600-B-H Instructions* (2000)

[42] Tirira J. and Trocellier P., 'Elastic recoil detection analysis', *Journal of Radioanalytical and Nuclear Chemistry*, **130**, 311 (1989)

[43] Golczewski A., Dobes K., Wachter G., Schmid M. and Aumayr F., ‘A Quartz-Crystal-Microbalance Technique to Investigate Ion-Induced Erosion of Fusion Relevant Surfaces’, *Nuclear Instruments and Methods in Physics Research B*, **267**, 695 (2009)

[44] Sugiyama K. (2015), private communication, manuscript in prep.

[45] Oberkofler M., Alegre D., Aumayr F., Brezinsek S., Dittmar T., Dobes K., Douai D., Drenik A., Köppen M., Kruezi U., Linsmeier C., Lungu C., Meisl G., Mozetic M., Porosnicu C., Rohde V. and Romanelli S., ‘Plasma–wall interactions with nitrogen seeding in all-metal fusion devices: Formation of nitrides and ammonia’, *Fusion Engineering and Design*, **98–99**, 1371 (2015)

Danksagung

Als Erstes möchte ich mich bei meinen Eltern, Elfriede und Fritz bedanken. Auch wenn ich nicht die Leidenschaft für landwirtschaftliche Tätigkeiten aufweise, haben Sie mich immer bei meinen karrieretechnischen Entscheidungen unterstützt.

Als nächstes bedanke ich mich ganz herzlich bei Prof. Dr. Friedrich Aumayr, da ich mit dieser Arbeit die Möglichkeit bekam einen kleinen Beitrag zur Fusionsforschung zu leisten. Weiters ist mir sein Optimismus und auch die scheinbare Leichtigkeit beim Herangehen an das Lösen von schwierigen physikalischen Problemen ein großes Vorbild. Es war eine sehr spannende Zeit und insbesondere die Chance auch an internationalen Forschungsaufenthalten und Konferenzen teilzunehmen war sehr lehrreich.

Weiters habe ich sehr viel von der Betreuung durch Bernhard Berger profitiert, dessen Korrekturen und kritisches Denken mir zugleich Hilfe als auch Motivation waren. Seine enorme Leidenschaft technische Probleme zu lösen und seine beinahe kindliche Begeisterung danach wird mir immer in Erinnerung bleiben.

Zuletzt möchte ich mich bei all den KollegInnen der Arbeitsgruppe Atom und Plasma Physik bedanken, insbesondere bei Elisabeth Gruber, Janine Schwestka und Florian Laggner. Eure Hilfsbereitschaft und auch die vielen sinnvollen und sinnfreien Konversationen waren sehr bereichernd.